Modeling the Role of Compaction in the Three-Dimensional Evolution of Depositional Environments

Journal of Geophysical Research: Earth Surface

Xotta, R.; Zoccarato, C.; Minderhoud, P.S.J.; Teatini, P.

https://doi.org/10.1029/2022JF006590

JGR Earth Surface

RESEARCH ARTICLE
10.1029/2022JF006590

Modeling the Role of Compaction in the Three-Dimensional Evolution of Depositional Environments

R. Xotta[1], C. Zoccarato[1], P. S. J. Minderhoud[1,2,3], and P. Teatini[1]

[1]Department of Civil, Environmental and Architectural Engineering, University of Padova, Padova, Italy, [2]Soil Geography and Landscape Group, Wageningen University, Wageningen, The Netherlands, [3]Department of Subsurface and Groundwater Systems, Deltares Research Institute, Utrecht, The Netherlands

Key Points:

- Auto-compaction represents an important process driving evolution, aggradation, and progradation of depositional landforms
- A novel three-dimensional model allows quantification of sediment compaction in complex, heterogeneous depositional environments
- Scenarios for the resilience of depositional landforms should not neglect compaction in long-term predictions

Supporting Information:

Supporting Information may be found in the online version of this article.

Correspondence to:

P. Teatini,
pietro.teatini@unipd.it

Citation:

Xotta, R., Zoccarato, C., Minderhoud, P. S. J., & Teatini, P. (2022). Modeling the role of compaction in the three-dimensional evolution of depositional environments. *Journal of Geophysical Research: Earth Surface*, *127*, e2022JF006590. https://doi.org/10.1029/2022JF006590

Received 5 JAN 2022
Accepted 22 AUG 2022

Author Contributions:

Conceptualization: C. Zoccarato, P. S. J. Minderhoud, P. Teatini
Funding acquisition: P. Teatini
Investigation: R. Xotta, P. Teatini
Methodology: R. Xotta, C. Zoccarato, P. S. J. Minderhoud, P. Teatini
Software: R. Xotta
Writing – original draft: R. Xotta
Writing – review & editing: R. Xotta, C. Zoccarato, P. S. J. Minderhoud, P. Teatini

Abstract Natural environments such as coastal wetlands, lowland river floodplains, and deltas are formed by sediment, transported by watercourses and the sea, and deposited over century to millennium timescales. These dynamic environments host vulnerable ecosystems with an essential role for biodiversity conservation, coastal protection and human activities. The body of these landforms consists of unconsolidated sediments with high porosity and compressibility. Consequently, they often experience significant compaction due to their own weight, that is, autocompaction, which creates an important feedback within the geomorphological evolution of the landform. However, this process is generally oversimplified in morphological simulators. We present a novel finite element (FE) simulator that quantifies the impact of natural compaction on landform evolution in a three-dimensional setting. The model couples a groundwater flow and a compaction module that interact in a time-evolving domain following landform aggradation. The model input consists of sedimentation varying in time, space and sediment type. A Lagrangian approach underlies the model by means of an adaptive mesh. The number of FEs gradually increases to accommodate newly deposited sediments and each FE changes its shape, that is, becomes compressed, following sediment compaction. We showcase the model capabilities by simulating three long-term depositional processes at different spatial scales: (a) vertical growth of a tidal marsh, (b) infilling of an oxbow lake, and (c) progradation of a delta lobe. Our simulations show that compaction is the primary process governing the elevation and geomorphological evolution of these landforms. This highlights that autocompaction is an important process that determines the resilience of these low-lying landforms to climate change.

Plain Language Summary Coastal wetlands, lowland river floodplains, and deltas are lowly elevated landforms. Their subsurface consist of sediments like sand, clay, and peat, which can by highly compressible. When they become buried by new sediments, which adds weight to the surface, the underlying sediments become increasingly compacted. While potentially highly influential, this process is generally neglected or oversimplified in morphological modeling. We developed a novel model that includes not only sedimentation and landform evolution in a three-dimensional domain, but sediment compaction. The model resolves the dynamic feedbacks between subsurface processes and morphological change and processes at the surface, such as sediment deposition, compaction and landform evolution. We apply the model to three different geomorphological cases: a growing tidal marsh, infilling of an oxbow lake, and aggradation and progradation of a delta lobe. Our results underscore the importance of sediment compaction on landform evolution.

1. Introduction

Coastal landscapes like coastal plains and river deltas are complex and dynamic depositional environments. They were formed over the last centuries to millennia by the deposition of inorganic and organic sediments transported seaward by rivers and delivered by flooding or produced by the decomposition of the local vegetation (Milliman & Farnsworth, 2011; Mudd et al., 2009). These dynamic environments are widespread around the world and play important socio-economic and ecological roles. They host industrial and agricultural activities, megalopolises with tens million inhabitants (Ericson et al., 2006; Seto, 2011), and also pristine natural environments considered the Earth's richest ecosystems and fundamental for biodiversity preservation (Barbier et al., 2011; Schindler et al., 2016). They host landforms such as wetlands, marshes, lagoons, oxbow lakes, and backswamps, which flood periodically or are permanently inundated, resulting in waterlogged soil conditions (Bridge, 2003; Dunne & Aalto, 2013). Their evolution is fundamentally controlled by the balance between the creation and filling of available three-dimensional (3D) accommodation space, as controlled by antecedent topography, tectonics, sea-level

changes, floods, sediment fluxes, tidal and wave regimes, and coastal and river hydrodynamics (Allen, 2000; Davis, 2013). A number of publications and models have been developed over the last decades on lowland river floodplain and coastal morphodynamic evolution aimed at understanding and predicting, for example, the progradation and aggradation of delta lobes (Kim et al., 2009; Moodie et al., 2019), the meander evolution and oxbow lake filling (Bogoni et al., 2017; Constantine et al., 2010), and the response of coastal wetlands to rising sea level (Fagherazzi et al., 2021; Marani et al., 2010).

Although neglected in the large majority of the morphodynamic models, post-depositional consolidation of the sediments due to the weight of their own overburden (also referred to as "autocompaction") can play an important role on landform evolution, with considerable consequences on, for example, its resilience to climate change (Allen, 1999; Brain, 2016; van Asselen et al., 2011). In fact, shallow newly formed deposits undergo a remarkable amount of compaction (Jankowski et al., 2017; Törnqvist et al., 2008; Zoccarato et al., 2020) because of their very large porosity and compressibility (Brain et al., 2015; Bridgeman, 2018). As new sediments deposit over a landform surface, the thickness of the underlying soil progressively decreases with a porosity reduction due to the gravitational load of the overburden (Brain et al., 2012; Zoccarato & Da Lio, 2021). Furthermore, as consolidation follows the dissipation of the pore-water overpressure (i.e., groundwater pressure above the hydrostatic distribution) caused by the new load (following the well-known Terzaghi's principle of the effective stress (Terzaghi, 1923)), compaction can last much longer than the deposition time frame depending on the hydraulic conductivity of the soil.

There are multiple practical consequences of sediment compaction on the geomorphology and evolution of depositional landforms. For example, the mass of sediments composing a certain 3D sedimentary body (e.g., a marshland or a delta lobe) is largely underestimated if obtained as the product by its (geometric) volume and the density (and porosity) of surficial soil samples (Bahr et al., 2001). Neglecting or misunderstanding compaction of tidal marsh sediments provides erroneous reconstructions of past sea-level evolution as highlighted by Brain et al. (2015). Furthermore, compaction implies that the amount of sedimentation required for a tidal marsh to build elevation and keep up with relative sea-level rise (SLR) will be larger if the marsh is composed of (more compressible) organic soil rather than (stiffer) silty-sands (Zoccarato & Teatini, 2017).

Several approaches have been developed recently to estimate natural compaction of Holocene sedimentary sequences. They are mainly based on empirical relationships (Allen, 1999; Sheldon & Retallack, 2001; van Asselen et al., 2009) or 1D compression models (Brain et al., 2012; Massey et al., 2006; Meckel et al., 2007; Mudd et al., 2009; Tovey & Paul, 2002). More advanced developments are available in the context of stratigraphic basin modeling. A mathematical model for the non-equilibrium compaction of clays in sedimentary basins is proposed by Audet and Fowler (1992). The model reduces to a generalized consolidation equation that, for the classical Darcy flow, is a non-linear diffusion equation for the porosity with a free boundary. Syvitski and Hutton (2001) developed SEDFLUX, a 2D basin-fill simulator to predict delivery and redistribution of a multi-sized sediment load onto and across a continental margin. Sediment compaction is accounted for through an exponential law dependent on the overburden load. With this work we aim to advance these previous efforts and (a) present the development of a novel 3D model called NATSUB3D, coded as a FORTRAN program, that properly accounts for sediment compaction during the 3D evolution of depositional landforms, (b) quantitatively highlight the role played by sediment compaction on the dynamics of landform evolution and elevation, and quantify autocompaction evolution based on the overpressure dissipation over time and space as governed by sediment properties and sedimentation rates.

NATSUB3D is 3D finite element (FE) simulator built by coupling a 1D geomechanical module based on the Terzaghi approach with a 3D groundwater flow module in the context of large (i.e., not infinitesimal) vertical motion of soil grains (Gambolati, 1973a). Using a Lagrangian approach, the landform evolution is simulated through (a) a deposition mechanism, with the sedimentation rate representing a condition on the upper boundary of the model domain and new elements added on this surface when the amount of sediments exceeds a threshold value; and (b) a consolidation mechanism accounting for soil compaction with node positions updated at each time step. The size of the time step varies to optimize the computational performance and properly manage sedimentation rates that can vary several orders of magnitude over time and space. The geomechanical properties of the soils are characterized by a nonlinear elasto-plastic constitutive model.

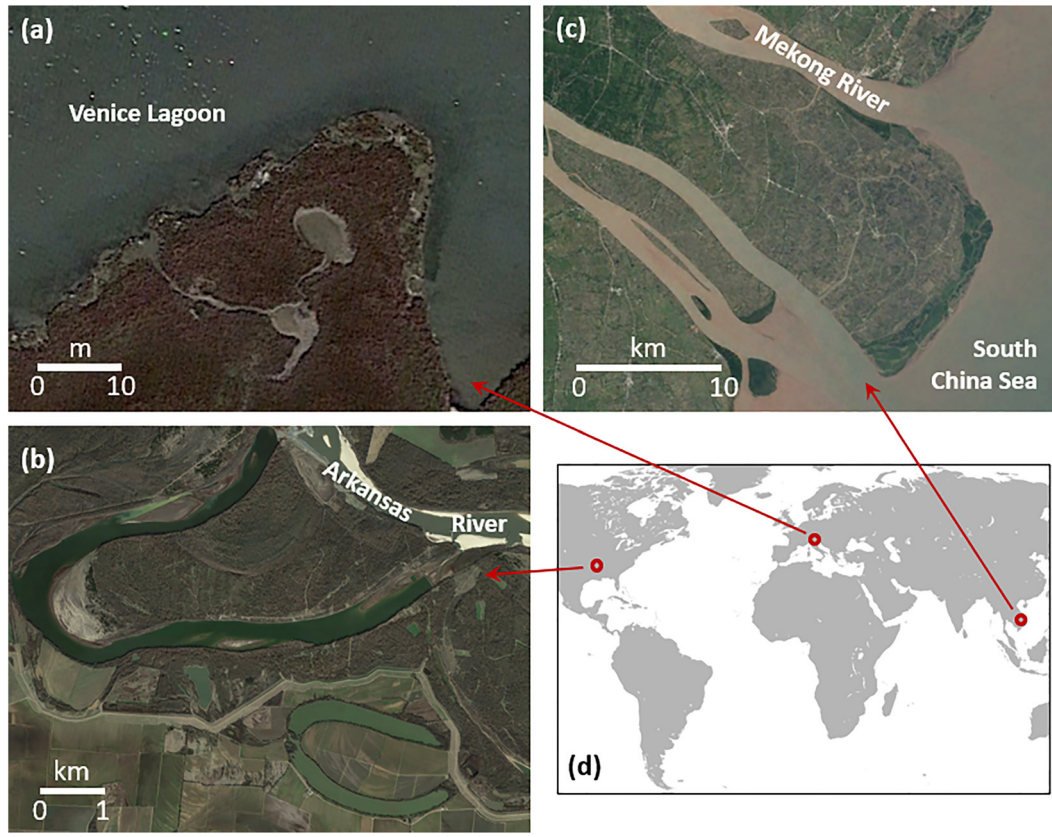

Figure 1. Satellite images of typical depositional environments used as examples for model simulation: (a) a tidal marsh in the Venice Lagoon, Italy; (b) oxbow lakes of the Arkansas River, Arkansas; (c) a delta lobe of the Mekong River, Vietnam. The site locations are shown in (d). Satellite images from Google Earth.

The model has been implemented starting from the former NATSUB2D model developed by Zoccarato and Teatini (2017) and applied to a representative vertical section of a tidal marsh in the Venice Lagoon, Italy (Zoccarato et al., 2019), and a transect in the Mekong Delta, Vietnam (Zoccarato et al., 2018). With the introduction of the third dimension, the potential to simulate the evolution of typical depositional landforms (e.g., as shown in Figure 1) as it occurs in nature is considerably enhanced. The coupling between the sedimentation process, whose dynamics is intrinsically 2D (Cosma et al., 2021; Pietroń et al., 2018), and the areal and depth variability of the hydro-geomechanical properties of sedimentary bodies requires the use of a 3D modeling analysis to be fully captured (Amorosi et al., 2020; Chamberlain et al., 2018). In fact, as depositional landforms are 3D soil bodies, a comprehensive picture of their evolution and a more complete representation of the overpressure dissipation field can be captured better using a modeling approach with the same dimensionality.

First we present the modeling approach, discuss the governing partial differential equations, the constitutive relationships and the numerical implementation. Then, the numerical solution obtained by NATSUB3D is validated against the outcome of the former 2D model by Zoccarato and Teatini (2017) and a convergence analysis on space and time dicretization is carried out to demonstrate the accuracy of the 3D model implementation. Subsequently, the model is used to simulate the geomorphological landform evolution and compaction that take place during three typical depositional processes: vertical elevation growth of a tidal marsh following SLR, the infilling of an oxbow lake, and the progradation of a delta lobe including beach ridge formation. The simulations do not refer to specific real-world cases, but we have elected to analyze realistic geomorphological settings, with proper hydro-geomechanical properties of the typical sediments composing Holocene landforms derived from the literature.

2. Modeling Approach

The methodological approach developed in this work is presented in the next sections. The mathematical model is first introduced in brief, as it represents a generalization of previous equations developed for 1D and 2D settings. Then, the principle constitutive relationships describing how the main hydro-geomechanical features, that is, compressibility, porosity, and hydraulic conductivity, vary with the effective stress are presented. Finally, the procedure developed to integrate the mathematical equations through FE in a 3D evolving domain is described in detail.

2.1. Governing Equations

Modeling the role of compaction in the long-term evolution of recently deposited landforms requires quantifying the relationship between the time and space distribution of the sedimentation rate ω and the dissipation of the water overpressure p, that is, the incremental pore pressure with reference to the hydrostatic condition within the porous body.

When describing the evolution of a sedimentary landform undergoing pronounced soil compaction, that is, a compaction larger than 5% of the landform initial thickness (Gambolati, 1973b), the vertical solid grain displacements should be taken into account. The behavior of autocompaction with time is governed by the dissipation of the groundwater overpressure that develops during the sedimentation process. The rigorous equation of groundwater flow in an elastic saturated porous medium undergoing large compaction was originally proposed in a 1D setting by Gambolati (1973a). It was revisited by Gibson et al. (1981) and lately updated again by Gambolati et al. (1998) to incorporate changes in total stress following deposition of new sediments on the top of the soil column as proposed by Gibson (1958) and Bredehoeft and Hanshaw (1968). The model by Gambolati et al. (1998), which was discussed against the formulation by Gibson (1958) and Bredehoeft and Hanshaw (1968) not accounting for nonlinearities arising from large deformations, was recently extended to a 2D domain by Zoccarato and Teatini (2017). In this work we generalize the formulation to a 3D setting, with the 3D groundwater flow equation solved within a landform evolving in time and space. The model needs to account for the geometric non-linearity that arises from the large solid grain movements. Therefore, Darcy's law is derived in terms of the relative velocity of fluid with respect to moving grains. For deformation, the vertical component (i.e., compaction) is considered since horizontal grain movements are negligible in shallow depositional environments subject to gravity only.

Generalizing Zoccarato and Teatini (2017), the governing equation of the groundwater flow in a 3D porous system undergoing large deformations can be written as:

$$\nabla \cdot \left(\frac{K}{\gamma} \nabla p \right) = (c_b + \phi\beta)\, Dp - c_b\,(1-\phi_0)\,(\gamma_s - \gamma)\,\omega \tag{1}$$

where:

1. $K = [K_x(\sigma_z), K_y(\sigma_z), K_z(\sigma_z)]$, with K_x, K_y, and K_z the components of the hydraulic conductivity tensor along the principal anysotropy directions. Generally, z coincides with the vertical direction, positive upward, x and y are two orthogonal horizontal directions;
2. σ_z the vertical effective stress;
3. γ the specific weight of water;
4. $c_b(\sigma_z)$ the oedometric soil compressibility;
5. $\phi(\sigma_z)$ the soil matrix porosity, with ϕ_0 the value at the land surface (where $\sigma_z \simeq 0$);
6. β the volumetric compressibility of water;
7. D the total (or Eulerian) derivative, $D = \frac{\partial p}{\partial t} + v_{g,z}\frac{\partial p}{\partial z}$, with $v_{g,z}$ the vertical grain velocity;
8. t is time.

The parameters K_x, K_y, K_z, ϕ, and c_b are dependent on the vertical effective stress.

The Lagrangian approach (Gambolati et al., 1998) underlies the numerical solution of Equation 1, where a dynamic mesh is employed: the grid nodes follow the grains movement caused by consolidation and, as a consequence, FEs deform. Indeed, over a moving node the Eulerian derivative Dp can be treated as a partial time

derivative $\partial p/\partial t$. The FE discretization approach used to solve Equation 1 leads to a system of non-linear ordinary differential equations solved by a back Euler method in time with a fixed-point iteration scheme.

In the context of depositional landforms, soil compaction is caused by the accumulation of new sediments on the ground surface. For a certain time interval Δt and sedimentation rate ω, the increase of the geostatic load $\Delta\sigma_t$ can be expressed as:

$$\Delta\sigma_t = (1-\phi_0)(\gamma_s-\gamma)\omega\Delta t \tag{2}$$

$\Delta\sigma_t$ represents the external factor causing the pore pressure to change with respect to the equilibrated hydrostatic distribution, as evidenced in the right-hand side of Equation 1. Pressure change p, increase of the geostatic load $\Delta\sigma_t$ and vertical effective stress $\Delta\sigma_z$ are related through the well-known Terzaghi's principle (Terzaghi, 1923). The shortening of a ℓ-thick soil column is caused by $\Delta\sigma_z$ (Gambolati, 1973a):

$$\Delta\ell = \alpha\ell\Delta\sigma_z \tag{3}$$

with α the classical soil compressibility, which is related to c_b by Gambolati et al. (1998):

$$c_b = \frac{p\frac{d\alpha}{dp}+\alpha}{1+\alpha p} \tag{4}$$

More generally, compaction $u(z, t)$ of a soil column extending from the basement ($z = 0$) to elevation z reads (Gambolati et al., 1998):

$$u(z,t) = -\int_0^z \frac{\alpha(\sigma_z)\sigma_z}{1-\alpha(\sigma_z)\sigma_z}dz \tag{5}$$

2.2. Constitutive Relationships

The vertical soil compressibility is considered to be the most fundamental mechanical parameter controlling the soil compaction. c_b is estimated thorough oedometer laboratory tests on soil samples by relating the variations of void ratio, e, and effective stress σ_z:

$$c_b = -\frac{1}{1+e}\frac{de}{d\sigma_z} \tag{6}$$

with $e = \phi/(1-\phi)$.

Equation 6 highlights how the assumption of constant c_b has validity over a limited range of σ_z. The porous medium becomes stiffer as σ_z increases and compaction progresses, and this is particularly evident at low effective stress, that is, for shallow soils. Obviously, c_b depends on the sediment types too. Notice that c_b is related to the compressibility index C_c provided by the usual graphical interpretation of oedometric tests through the relationship:

$$c_b = \frac{1}{ln10}\frac{C_c}{(1+e)\sigma_z} \tag{7}$$

being C_c a parameter depending on sediment type only, at least in the depth (and vertical effective stress) range of interest. C_c must be substitute by the re-compression index C_r if $\sigma_z < \sigma_{z,c}$, with $\sigma_{z,c}$ the preconsolidation stress, that is, the maximum vertical effective stress experienced by the soil. The constitutive relationships linking e to σ_z through re-compression and compression indices are the following:

$$e = \begin{cases} e_0 - C_r\log\left(\frac{\sigma_z}{\sigma_{z0}}\right), & \sigma_z < \sigma_{z,c} \\ e_c - C_c\log\left(\frac{\sigma_z}{\sigma_{z,c}}\right), & \sigma_z \geq \sigma_{z,c} \end{cases} \tag{8}$$

where e_0 and σ_{z0} are the void ratio and the effective stress at very shallow depth, e_c is the void index at the preconsolidation stress. As we simulate the landform evolution since its origin, σ_z is equal to $\sigma_{z,c}$ suggesting the use of the

second equation in Equation 8 only. However, we introduce a minimum value of the preconsolidation stress $\sigma_{z,\mathrm{pre}}$ to account for other processes that can affect soil compressibility rather than consolidation due to overpressure dissipation. This overconsolidation state (i.e., $\sigma_z < \sigma_{z,\mathrm{pre}}$) has been witnessed in the field, for example, it was quantified for a shallow marsh soils by Brain et al. (2011) and ascribed to the "results from desiccation and capillary suction stresses caused by varying degrees of subaerial exposure, falls in groundwater level and the moisture requirements of vascular plants." By means of Equation 8, the geomechanical behavior of various sediments is fully defined by the two parameters e_0 and C_c (or C_r). Compression and re-compression indices have been widely reported for many different types of soils across the globe (Mesri & Vardhanabhuti, 2009). Once e-vs-σ_z is available, c_b is quantified for various stress values using Equation 7.

As to the hydraulic conductivity, the following relation is used (Lambe & Whitman, 1969):

$$K_z = K_{z_0}\, 10^{\left(\frac{e-e_0}{C_k}\right)} \tag{9}$$

with K_{z_0} the vertical hydraulic conductivity at e_0, that is, for a soil close to the land surface, and C_k a parameter related to lithology and void ratio (Terzaghi et al., 1996).

2.3. Numerical Implementation

Equation 1 is solved numerically through the FE method with a tetrahedral discretization. Managing a 3D FE mesh evolving in time and space in relation to the element number and the node number and coordinates is quite challenging. The main steps of the procedure implemented to this aim are described in the following.

The sedimentation thickness ($d\ell_i = \omega(x, t) \cdot \Delta t_i$) is initially computed to evaluate the soil deposited during the ith time step Δt_i. Notice that, if $d\ell_i$ exceeds a prescribed elemental thickness (i.e., the threshold value $\Delta z_{\max}$), Δt_i must be reduced to $\Delta t_i = \Delta z_{\max}/\omega$. Then, the total stress σ_t is updated (Equation 2) and a Picard iterative scheme is implemented to solve the system of nonlinear ordinary differential equations obtained by the numerical discretization of Equation 1. Once p^{k+1} is computed, where k is the counter of the nonlinear iteration, the approximate σ_z^{k+1} is calculated by Terzaghi's principle, $\sigma_z^{k+1} = \sigma_t - p^{k+1}$. σ_t is kept constant within each time step as its variation is only due to sediment accumulation on the landform surface. At each iteration, the hydro-geomechanical parameters of each element are updated using the constitutive relationships described above (Equations 7–9) and the actual depth interval Δz_i^{k+1} between two adjacent nodes is updated as follows:

$$\Delta z_i^{k+1} = \Delta z_i^0 + \Delta u_i^{k+1} \tag{10}$$

where Δz_i^0 is the depth interval at the previous time step and Δu_i^{k+1} its shortening computed using Equation 5 (Figure 2). When the difference between the solutions obtained in two consecutive iterations is smaller than a prescribed tolerance, the convergence is achieved.

The new $(i + 1)$ time step starts checking the need for mesh update. If the sediment thickness $\ell_{i+1} = \ell_i + d\ell_{i+1}$ above the generic node j exceeds the threshold thickness $\Delta z_{\max}$, a new node is added above j, that is, keeping the same x and y coordinates. Notice that $\Delta z_{\max}$ is subtracted from ℓ_{i+1} in view of the following time step. Consequently, a new tetrahedral element is built-up above each triangular face on the top surface sharing node j (Figure 2). The topology of the 3D tetrahedral mesh and the 2D triangulated surface of the landform are updated, together with the vectors containing the nodes on the top and possibly the lateral domain boundaries. The hydro-geomechanical parameters of the new elements are set equal to the properties of the proper sediment type at the shallowest depth. Once the total stress is re-computed, the $(i + 1)$ time step continues solving Equation 1 as described above.

The tetrahedral element mesh develops over time above a rigid reference layer representing, for example, the Pleistocene-Holocene sedimentary boundary or a rock unit above which sedimentary deposition takes place. The landform is approximated as fully saturated, consistently with the average near-surface groundwater table typical found in low-lying transitional environments.

Concerning boundary conditions of the modeling domain, the basement is assumed impermeable and the lateral/side surfaces can be either no-flow (Neumann condition) or with a fixed zero p (Dirichlet condition). Null Dirichlet conditions, which refer to hydrostatic pressure since p is the over-pressure relative to the hydrostatic distribution, are imposed also at the top boundary of the model. When accretion of new material above the surface

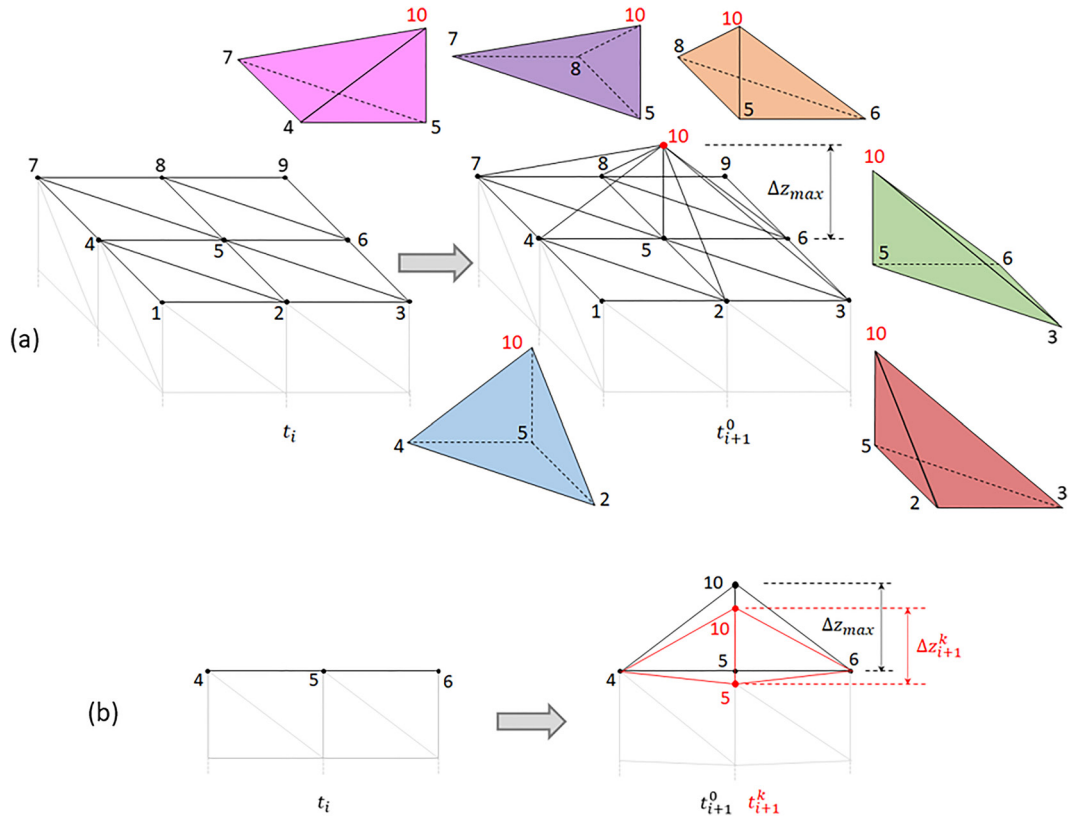

Figure 2. (a) Visualization of tetrahedra added at time t_{i+1} to the growing finite element mesh when the sedimentation thickness above node 5 reaches the prescribed thickness Δz_{max}. Adding node 10 implies to built-up new elements above those sharing node 5. In this example six new tetrahedra are added to the previous mesh. The new six elements are depicted individually and highlighted with different colors. The vectors containing the nodes on the top is updated from (1, 2, 3, 4, 5, 6, 7, 8, 9) at time t_i to (1, 2, 3, 4, 6, 7, 8, 9, 10) at time t_{i+1}. (b) Vertical section of the mesh through the alignment connecting nodes 4, 5, and 6 showing how the mesh deforms due to compaction because of the sedimentation Δz_{max} above node 5.

node reaches the threshold thickness (i.e., initial vertical element size), a new node is added above the actual model top and the boundary conditions need to be updated. The new node index substitutes the beneath one or the vectors with Neumann or Dirichlet nodes increases if the node is on a lateral boundary.

3. Validation and Convergence Analysis

3.1. Model Validation

The validity of the proposed 3D model is checked against the former 2D simulator published by Zoccarato and Teatini (2017). The two codes are used to simulate the formation and thickening of a 10-m wide sedimentary landform. The 3D model is obtained by extending the 2D domain for 3 m along the y direction (Figure 3). No-flux conditions are imposed on the lateral and bottom boundaries, with $p = 0$ on the land surface. The simulation spans 1,000 years using a 1-year time step. The spatial discretization is 0.1 m along the reference directions and the vertical element threshold (Δz_{max}) is also set to 0.1 m.

The sedimentation rate is uniform and equal to 3 mm/yr during the first 800 years and varies linearly with x between 0 and 3 mm/yr from 800 to 1,000 years. The deposited sediment is peat during the first 400 years, clay from 400 to 800 years, and silt over the last 200 years, mimicking a scenario in which a peatland becomes buried by clastic sediments, for example, following an encroaching river. The hydro-geomechanical properties of the various sediments used in this work are summarized in Table 1.

Figures 3a and 3b show the landform evolution at several key moments obtained by both the 2D and 3D models. Notice the uneven compaction characterizing the peat and clay layers at 1,000 years due the variable load exerted

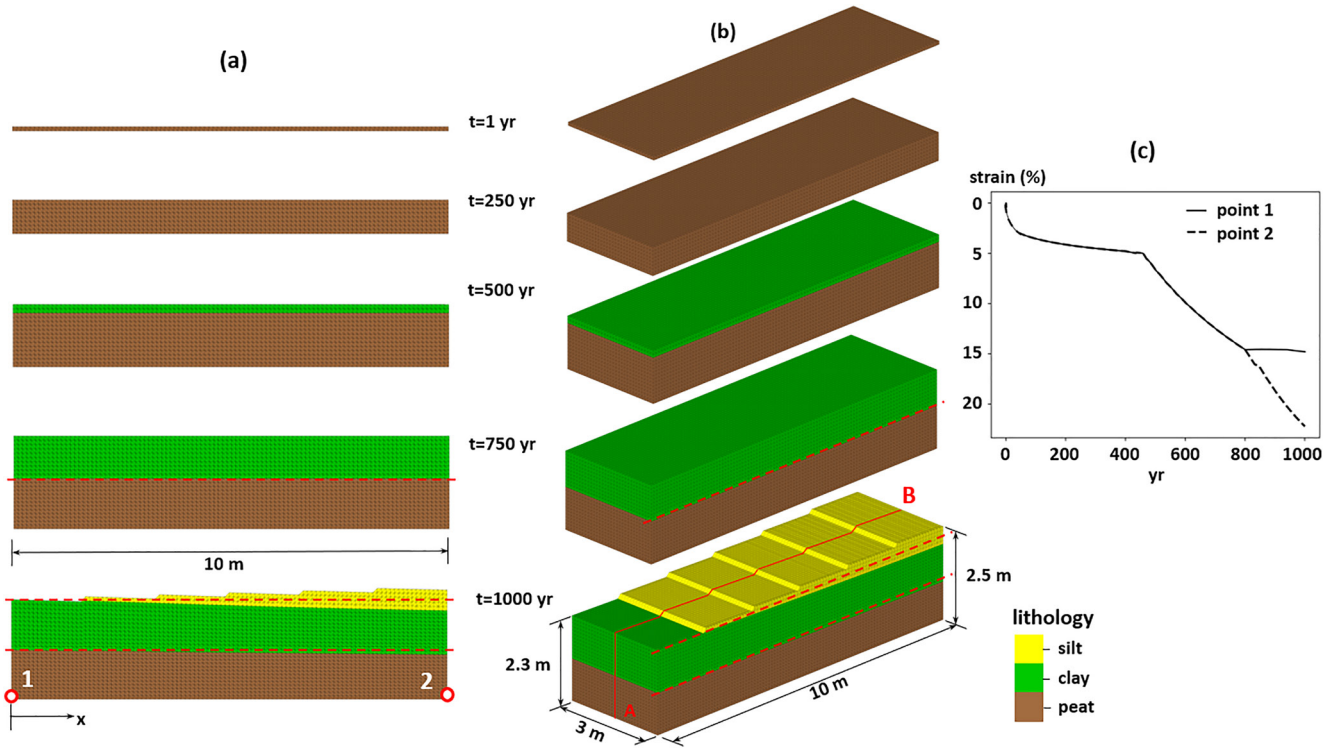

Figure 3. Evolution of the model domain including different sediment classes used to validate the proposed three-dimensional model: (a) 2D and (b) 3D models. The validation scenario simulates a potential real-world case in which initial peat deposition gradually becomes buried by floodplain (clay) and overbank deposits (silt). The colors represent the different sediment classes. The dashed red lines are horizontal references introduced to highlight uneven compaction at 1,000 years. The results of the 3D simulation are evaluated and compared to the 2D model on the AB transect highlighted in red. (c) Strain versus time for points #1 and #2 highlighted in (a), t = 1,000 years.

by the silt unit. At the end of the simulated period the effective stress σ_z on the model bottom ranges from 2.46 kPa at $x = 0$ m to 4.92 kPa at $x = 10$ m where 0.6 m thick silt layer deposited, with an overpressure averaging 0.167 kPa. Cumulative compaction amounts to 0.10 and 0.48 m at $x = 0$ m and $x = 10$ m, respectively.

The relative differences between the two model outcomes in terms of surface elevation ϵ_{ℓ}, overpressure ϵ_p, and effective stress ϵ_{σ_z} at the domain bottom are reported in Table 2. The difference is smaller than 1% (much smaller in most of the cases) ensuring that the 3D model results are consistent with those provided by the previous 2D approach.

Figure 3c shows the evolution versus time of the strain at the two points highlighted in Figure 3a. It is interesting to note the difference between the two after $t = 800$ years when sedimentation ends above point #1 and continues above point #2. Also notice the abrupt change of strain rate at $t \simeq 440$ years due to the rise of the stress above the $\sigma_{z,\text{pre}}$ value provided in Table 1.

Table 1
Hydro-Geomechanical Properties of Typical Sediment Classes Composing Depositional Landforms Used in This Work

Material ID	$\sigma_{z,\text{pre}}$ (kPa)	γ_s (kN/m^3)	e_0 (–)	C_c (–)	C_r (–)	K_z (m/s)	K_x/K_z, K_y/K_z (–)
Peat	1.0	20	15	4.0	0.40	10^{-7}	3.0
Clay	1.0	27	10	3.0	0.10	10^{-9}	3.0
Silt	1.0	27	3.0	0.5	0.05	10^{-7}	3.0
Sand	1.0	27	1.0	0.2	0.02	10^{-6}	3.0

Note. The values were derived after Brain et al. (2015), Bridgeman (2018), and Zoccarato et al. (2018). e_0 represents void ratio at $\sigma_z = \sigma_{z0} = 0.01$ kPa.

3.2. Convergence Analysis on Space and Time Discretization

A convergence analysis on the space and time discretization is carried out to test the accuracy of the 3D model implementation. Convergence is tested on the case study used in modeling validation (Figure 3), with the same domain size, sedimentation history, and material distribution. The modeling outcomes at 1,000 years and $y = 1.5$ m are considered.

Mesh convergence is checked by using a mesh size (both the x and y discretization and $\Delta z_{\max}$) equal to 0.05, 0.1, 0.2, and 0.4 m. Time step is equal to 1 year. A mesh size equal to 0.1 m is used to verify the time convergence. In

Table 2
Relative Difference Between the 2D and Three-Dimensional Model Outcomes in Terms of Elevation (ϵ_ℓ), Bottom Overpressure (ϵ_p) and Effective Stress (ϵ_{σ_z}) at x = 0 m, x = 5 m, and x = 10 m

x (m)	ϵ_ℓ	ϵ_p	ϵ_{σ_z}
0	8.7×10^{-5}	1.4×10^{-2}	4.8×10^{-3}
5	2.1×10^{-5}	4.5×10^{-4}	4.8×10^{-5}
10	1.7×10^{-3}	4.7×10^{-4}	1.1×10^{-2}

Note. The solution of the 3D model refers to the middle AB vertical section (i.e., at $y = 1.5$ m) pointed out in Figure 3b.

this case the following four values of the time step Δt are selected: 0.5, 1, 2, and 4 years.

The convergence is investigated by computing the relative difference of the surface elevation ϵ_ℓ obtained with the finest (space and time) discretization and the other space and time step values listed above. The result are summarized in Tables 3 and 4 for the space and time analyses, respectively. The ϵ_ℓ decrease with both the mesh size and time step guarantees the model convergence.

4. Results

We present three cases of examplar depositional landforms to show the potential of the proposed model that properly account for soil compaction during landform evolution in a 3D context. The cases represent three typical processes, that is, the vertical growth of a salt marsh to follow relative SLR (e.g., Bunzel et al., 2021), the filling of an oxbow lake (e.g., Toonen et al., 2012; Ishii & Hori, 2016), and the aggradation and progradation of a delta lobe (e.g., Chamberlain et al., 2018). Figure 1 shows real world examples of which we simulate the synthetic cases of landform evolution following sedimentation and compaction.

Although we do not simulate real world cases based on site-specific field data, the analyses are carried out using a realistic modeling set-up, that is, using configurations that summarize the typical geomorphological features with simplified geometries. The characteristic spatial scale ranges from a few tens of meters for a lagoon marshland, to hundreds of meters for a large oxbow lake and tens of kilometers for a delta lobe. The typical time scale of the simulated depositional processes and landform evolution ranges from a hundred to a few thousand years. The space and time behaviors of the sedimentation rate ω are specified beforehand using raster maps or analytical functions, which can both be specified as input data in the present version of the simulator. The sediment classes and properties are those reported in Table 1.

4.1. Case A: Thickening of a Tidal Marsh

Tidal marshes are dynamic environments driven by the interaction between surface processes (i.e., sedimentation, erosion, organic matter accumulation and degradation (Marani et al., 2010; Wiberg et al., 2020), and subsurface processes (i.e., soil consolidation (Brain et al., 2015; Zoccarato & Da Lio, 2021; Zoccarato et al., 2019)). Long-term evolution and resilience of such ecosystems are related to their capability to keep pace with long-term relative SLR, represented by SLR due to climate change and vertical land motion (or background subsidence) of bedrock or older Pleistocene sediments underlying the shallow unconsolidated Holocene deposits (Keogh & Törnqvist, 2019). On a medium to long-term scale, the thickness of the sedimentary body of a salt marsh usually increases over time (Bunzel et al., 2021; Weis, 2016) with a balance between (a) the net sedimentation of inorganic and organic soils on its surface reduced by autocompaction of the marsh sedimentary body, and (b) the sum of SLR and background subsidence.

The model is used to simulate the evolution of (a portion of) a salt marsh adjacent to a tidal creek following gradual relative SLR. The simulated domain extends 10 × 10 m in the horizontal plane, with a regular space discretization in both horizontal and vertical (Δz_{max}) of 0.1 m. No-flux conditions are imposed on the inner lateral and bottom boundaries, with $p = 0$ along the creek bank and on the land surface. The simulation spans a time interval equal to 3,000 years, with the sediment deposition characterized by three consecutive phases (Text S1 in Supporting Information S1 for sedimentation rate (ω) input maps):

- Growth of a peat land. From 0 to 1,000 years peat is accumulating with a ω of 1.5 mm/yr on the location of the marsh and 0.15 mm/yr in the creek;
- deposition of overbank deposits (silts) on top of the peat and the formation of a natural levee next to the creek, simulating increased tidal activity and sediment influx in the channel. Silt is deposited from 1,000 to 1,500 years on top of the marsh at a constant ω of 1.5 and 0.15 mm/yr in

Table 3
Convergence Analysis on Space Discretization: Relative Difference of the Surface Elevation ϵ_ℓ With Respect to the Model Solution Obtained With a Mesh Size Equal to 0.05 m

Δx (m)	$x = 0$ m	$x = 5$ m	$x = 10$ m
0.4	7.88×10^{-3}	1.16×10^{-1}	5.09×10^{-2}
0.2	3.23×10^{-3}	3.03×10^{-2}	3.68×10^{-2}
0.1	1.02×10^{-3}	3.38×10^{-3}	1.78×10^{-2}

Table 4
Convergence Analysis on Time Discretization: Relative Difference of the Surface Elevation ϵ_ℓ With Respect to the Model Solution Obtained With $\Delta t = 0.5$ years

Δt (yr)	$x = 0$ m	$x = 5$ m	$x = 10$ m
4	1.27×10^{-2}	1.61×10^{-2}	7.63×10^{-3}
2	6.91×10^{-4}	9.94×10^{-4}	7.94×10^{-4}
1	8.69×10^{-6}	1.75×10^{-4}	8.22×10^{-4}

the creek. From 1,500 to 2,000 years the formation of a natural levee is simulated by decreasing ω linearly from 1.5 to 0.15 mm/yr with distance from the creek. Sedimentation in the creek has stopped;

- continued salt marsh growth following the accumulating finer grained sediments (clay) and organic matter, simulating the change to a lower energetic environment and sediment influx. During the last thousand years of the simulation (from 2000 to 3000 years) $\omega = 1.5$ mm/yr on the salt marsh with the exception of a central pond receiving reduced sedimentation ($\omega = 0.5$ mm/yr).

The model results are shown in Figures 4 and 5. Figure 4 shows an axonometric view of the simulated salt marsh evolution at four relevant time steps. In total, the number of model elements in the domain increases from 60,000 (with 20,402 nodes) at the beginning of the simulation (when only a single FE layer representing the marsh basement composes the mesh) to 2,144,131 (and 362,971 nodes) at $t = 3{,}000$ years. The maximum marsh thickness of 3.8 m is reached adjacent to the tidal creek. This thickness is considerably smaller than the product of the sedimentation rate (equal to 1.5 mm/yr along the marsh boundary times 3,000 years deposition time, totaling 4.5 m) as a result of soil compaction (0.7 m for the column). Figure 5 shows the model outcomes in terms of marsh thickness and sediment distribution versus depth, overpressure, and strain ϵ along a vertical section orthogonal to the tidal creek (alignment AB in Figure 4). Notice how overpressure (p) develops during the sedimentation of the clay layer toward the end of the simulation, while p remained negligible until $t = 2{,}250$ years. The increased values of p primarily develop inside the clay layer as its hydraulic conductivity is much smaller than that of the other sediment types (Table 1). Additionally, p also increases in the underlying peat and silt deposits in the inner part of the marsh (Figure 5, left side) with increasing distance from the creek: here groundwater pressure is equilibrated with the creek water pressure (where hydrostatic distribution has been imposed as boundary condition) but it cannot dissipate from the other side boundaries where a no-flow condition is imposed because of the domain symmetry. Notice also that an overpressure gradient develops along the horizontal direction too, mainly around the pond and in proximity of the tidal creek, showing that the groundwater flow pattern is 3D. Soil compaction is related to the geostatic load and the intrinsic compressibility of each sediment type. These two factors contribute to get the maximum strain, up to 31%, in the peat layer. Compaction decreases to about 10% in the intermediate silty unit and vanishes moving upward within the clayey layer.

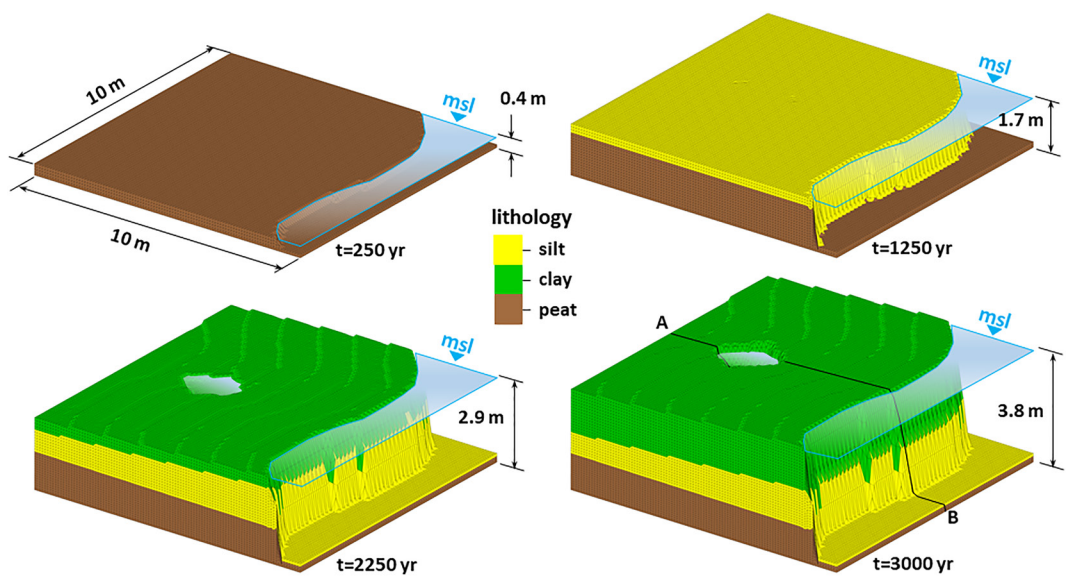

Figure 4. Tidal salt marsh evolution at times 250, 1,250, 2,250, and 3,000 years. The simulated salt marsh borders a tidal creek. The colors represent the different sediment types.

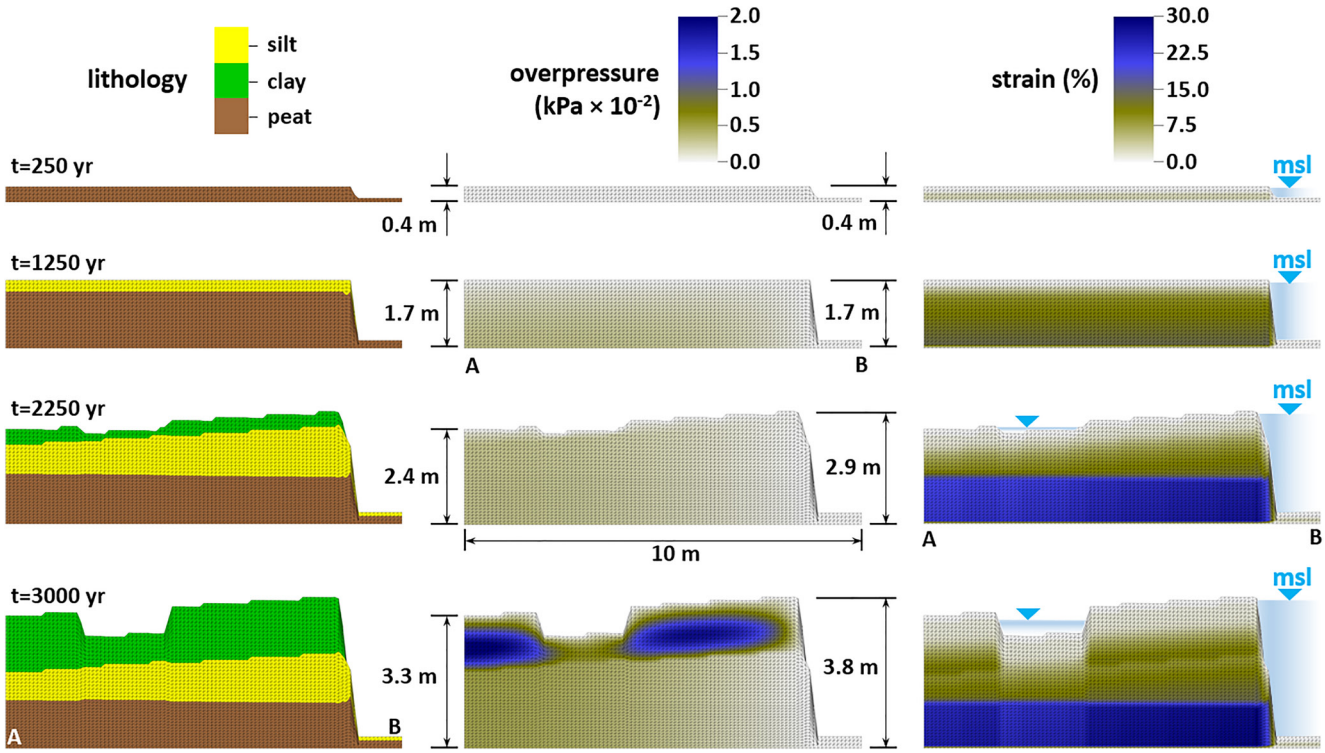

Figure 5. Tidal marsh evolution: sedimentology, overpressure, and strain along the vertical section traced in Figure 4 at times 250, 1,250, 2,250, and 3,000 years.

4.2. Case B: Filling of an Oxbow Lake

Oxbow lakes are widespread and distinctive landforms within fluvial landscapes. They form when an active river channel becomes disconnected and abandoned following a meander cutoff. The initial formation of plug bars at the meander entrances is followed by a progressive filling (i.e., shallowing and narrowing) during the channel abandonment (Bogoni et al., 2017). The sedimentary architecture of these fills depends on the sediment type and deposition conditions (Constantine et al., 2010), with layering being a main feature of oxbow lake infills. Alternations of fine clastic sediments (silt and clay) and sediments rich in organic matter represent different stages of flooded or vegetated meander conditions (Toonen et al., 2012), with clastic sediments being deposited at higher rates (flood-based) than organic sediments produced in situ (Minderhoud et al., 2016). This process may last from many decades to several millennia, depending on the rate of sediment supply (Hudson & Kesel, 2000; Ishii & Hori, 2016; Minderhoud et al., 2016).

In the present modeling framework, we simulate the filling of an oxbow lake (Figure 6). Text S2 in Supporting Information S1 provides the equations used to mathematically define the abandoned channel within a sandy alluvial plain. This topographical setting schematically represents the initial configuration of the oxbow lake, which is 30 m wide at the land surface and ∼2.1 m deep. The initial model domain, which is 100 × 100 m wide and ∼2.6 m thick, is discretized by a 3D mesh composed of 255,056 nodes and 1,480,505 tetrahedra. The characteristic element dimension is 1.0 m in the horizontal plane and Δz_{max} equals 0.1 m. No-flux conditions are imposed on the lateral and bottom boundaries, with $p = 0$ on the land surface. Infilling of the lake lasts 2,000 years and is comprised of a sequence of alternating peat and clay layers that change every 200 years. The equations used to describe the space distribution of ω are reported in Text S3 in Supporting Information S1. A uniform silt layer deposits over the last 100 years with $\omega = 5$ mm/yr simulating the deposition of overbank deposits on top of the infill. The final mesh consists of 365,028 nodes and 2,146,932 elements.

Figure 6 shows a 3D representation of the domain evolution and the various sediment types. Four representative times are shown, respectively: the initial shape of the oxbow lake at $t = 0$ years, the infilling conditions after 500 and 1,500 years, and the final setting at $t = 2{,}100$ years. The model outcomes in terms of domain evolution, overpressure, and strain on the vertical section representing the symmetry plane of the domain (see alignment AB in

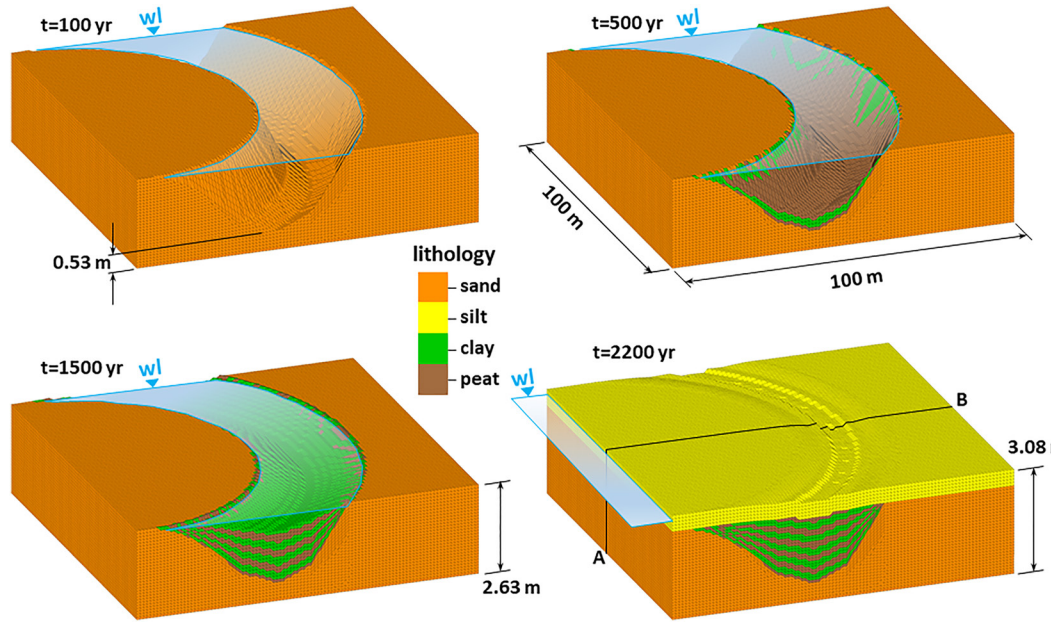

Figure 6. Infilling of an oxbow lake at times 0, 500, 1,500, and 2,100 years while properly accounting for sediment autocompaction. The colors represent the different sediment types. Vertical exaggeration is 10.

Figure 6) are shown in Figure 7. Overpressure develops mainly in the oxbow filling soils where low-permeable clay is deposited, while it is negligible in the sandy deposits because of their higher permeability. Notice also that the overpressure dissipates largely through the lake bottom, that is, along a sub-horizontal direction, since vertical flow is largely precluded by the clay layers. The oxbow fill furthermore compacts considerably, up to 20%, when it becomes loaded by the silty overbank deposits, causing a residual depression to form at the land surface at t = 2,100 years. Strain of the silty unit due to its own weight amounts to ~6%. Notice that the 2.6-m initial thickness of the sandy layer is the result of a prior application of the model before the infill started. The sand body itself also compacted due to its own weight, with a depth-averaged ϵ equal to 13%. Deposition of the upper silty layer increases compaction of the sand only slightly (~1%) due to its low compressibility (Table 1).

4.3. Case C: Aggradation and Progradation of a Delta Lobe

Deltas are the most dynamic coastal systems on Earth. They are large sedimentary deposits formed where rivers enter a standing water body. It is well-documented that, together with reductions in sediment supply (Syvitski et al., 2005) and accelerating rates of SLR (Ericson et al., 2006), compaction of Holocene shallow deposits triggered by their own weight is a major process contributing to rapid delta transformation (Liu et al., 2021; Teatini et al., 2011; Törnqvist et al., 2008; Zoccarato et al., 2018).

Delta progradation can amount to several tens of meters per year (e.g., 50 m/yr in the Mekong delta (Zoccarato et al., 2018) and 100–150 m/yr in the Lafourche subdelta of the Mississippi river (Chamberlain et al., 2018)), with thicknesses of the Holocene deposits ranging from a few meters (e.g., in the Danube (Vespremeanu-Stroe et al., 2017) and Chao Praya deltas (Tanabe et al., 2003)) to several tens of meters (e.g., in the Godavari (Nageswara Rao et al., 2015) and Mississippi deltas (Bridgeman, 2018)). Here, we simulate the aggradation of a schematic delta lobe over a period (T) of 1,000 years with a prodelta progradation rate (v_{pro}) of 10 m/yr and an active sedimentation phase (ΔT) lasting 250 years. The equations used to describe the space and time distribution of ω are provided in Text S4 in Supporting Information S1. Notice that the uncompacted delta plain thickness, which amounts to $\omega \times T$, is fixed at 11 m. We also simulate the formation of two 4-m high sandy beach ridges or foredunes over the periods between 500 and 600 years and from 900 to 1,000 years, respectively. Text S4 in Supporting Information S1 reports the related functions $\omega(x, y, t)$.

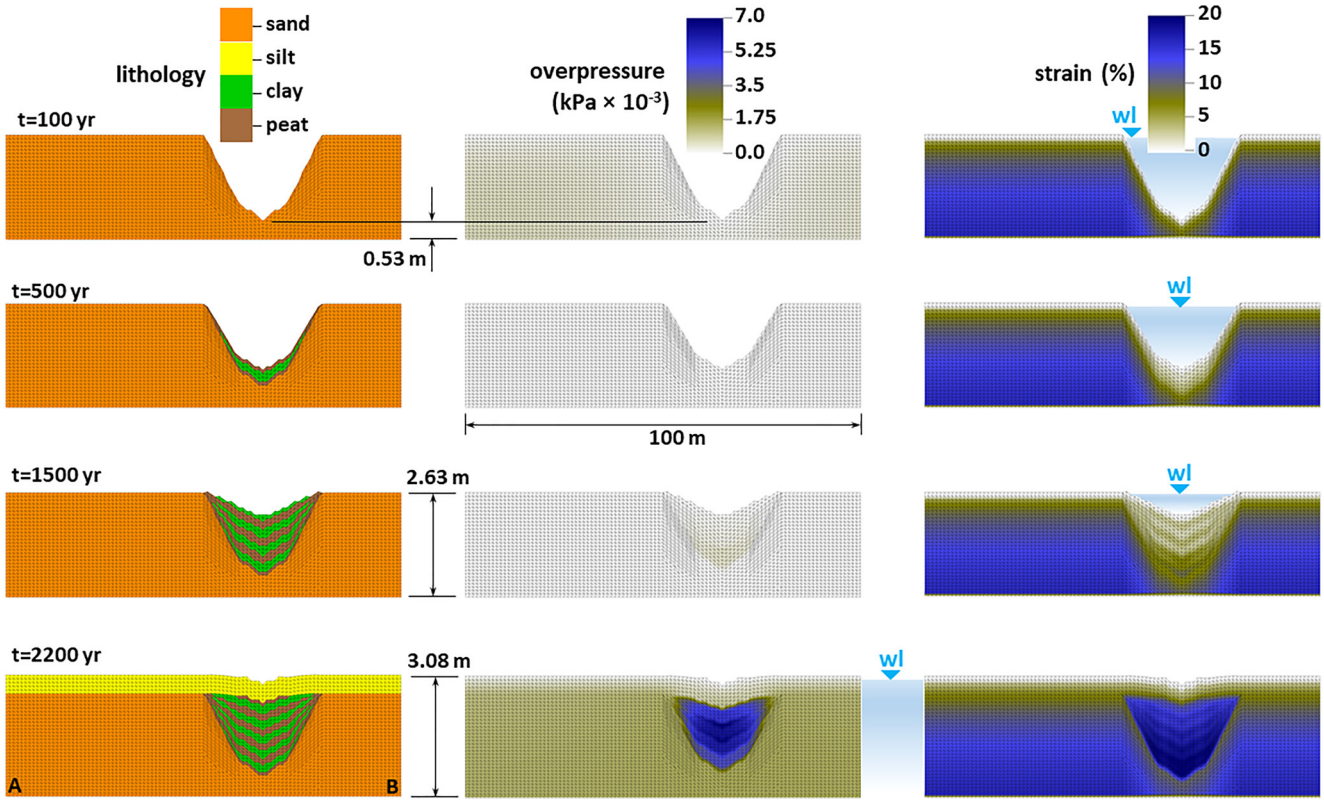

Figure 7. Oxbow lake evolution: sedimentology, overpressure, and strain along the vertical section traced in Figure 6 at times 100, 500, 1,500, and 2,200 years. Vertical exaggeration is 10.

Delta stratigraphy is generally characterized by a succession of various sediment types ranging from clay to silt and sand, with intercalated organic soils (Meckel et al., 2007). In the simulation here presented, we refer to the stratigraphy after Chamberlain et al. (2018), with a delta front made predominantly by clay on the bottom and silt on the top, above which mouth bar sands are deposited. The periods of clay, silt and sand deposition amount to $6/9\Delta T$, $2/9\Delta T$, and $1/9\Delta T$, respectively.

The horizontal model dimension extents 10 km along both the x and y directions. A regular space discretization equal to 100 m along x and y, with Δz_{max} equals 0.1 m are used. To reduce mesh distortion, a scale factor equal to 10^{-3} is applied along the horizontal directions. The values of K_x and K_y provided in Table 1 are scaled appropriately. The element number used to discretize the domain increases from 60,000 (and 20,402 nodes) at the beginning of the simulation (when only a single FE layer representing the lobe floor is considered) to 3,184,566 (and 534,034 nodes) at t = 1,000 years. No-flux conditions are imposed on the bottom and the vertical lateral boundary from which aggradation started, with $p = 0$ on the lobe surface.

Figure 8 shows the simulated domain at four moments in time, that is, t = 100 years, t = 500 years, t = 750 years, and t = 1,000 years showing the delta lobe progradation and the formation of beach ridges or foredunes on top. Notice that the final delta plain and ridge elevation amounts, respectively, to 7.7 and 10.1 m with a total compaction equal to 3.3 m (i.e., 30% of the uncompacted thickness) and 4.9 m (i.e., 33% of the uncompacted thickness). The average slope of the simulated prodelta is equal to 0.3%. Domain evolution, overpressure, and strain on the three vertical sections traced in Figure 8 are provided in Figures 9 and 10. Main outcomes to be highlighted are the following:

- The deformation of the deeper layers due to the load of the overlying sediments, with the dune ridges playing a major, although local, effect. This is particularly evident for the silt unit that, once deposited with a tabular shape, is bent by the shallowest sandy layer characterized by a highly variable thickness and, consequently, exerting a highly variable load;

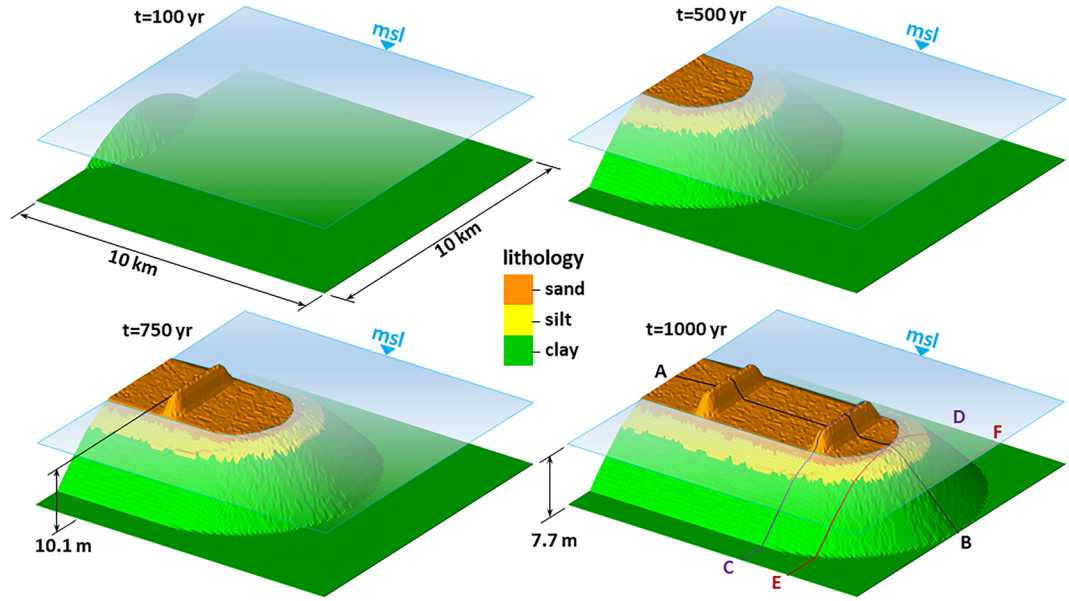

Figure 8. Simulated evolution of a delta lobe at times 100, 500, 750, and 1,000 years including the formation of two beach ridges or foredunes. The colors represent the different sediment classes. Vertical exaggeration is 250.

- the significant overpressure (up to 18 kPa) within the prodelta and nearby backward deposits where sedimentation is ongoing or the elapsed time is insufficient for dissipation. This overpressure is the cause of the notable difference between the surface elevation at the delta front shoreline ($\ell \simeq 8.0$ m) and the delta plain ($\ell \simeq 7.7$ m). The overpressure following sedimentation completely dissipates below the delta plain with a groundwater flow pattern that is characterized by a significant sub-horizontal component. Notice a certain difference between p in the clay unit below the older ($p \simeq 0$) and the more recent (p ranges from 2 to 4 kPa) dune ridges suggesting that more time is needed for a complete p dissipation;

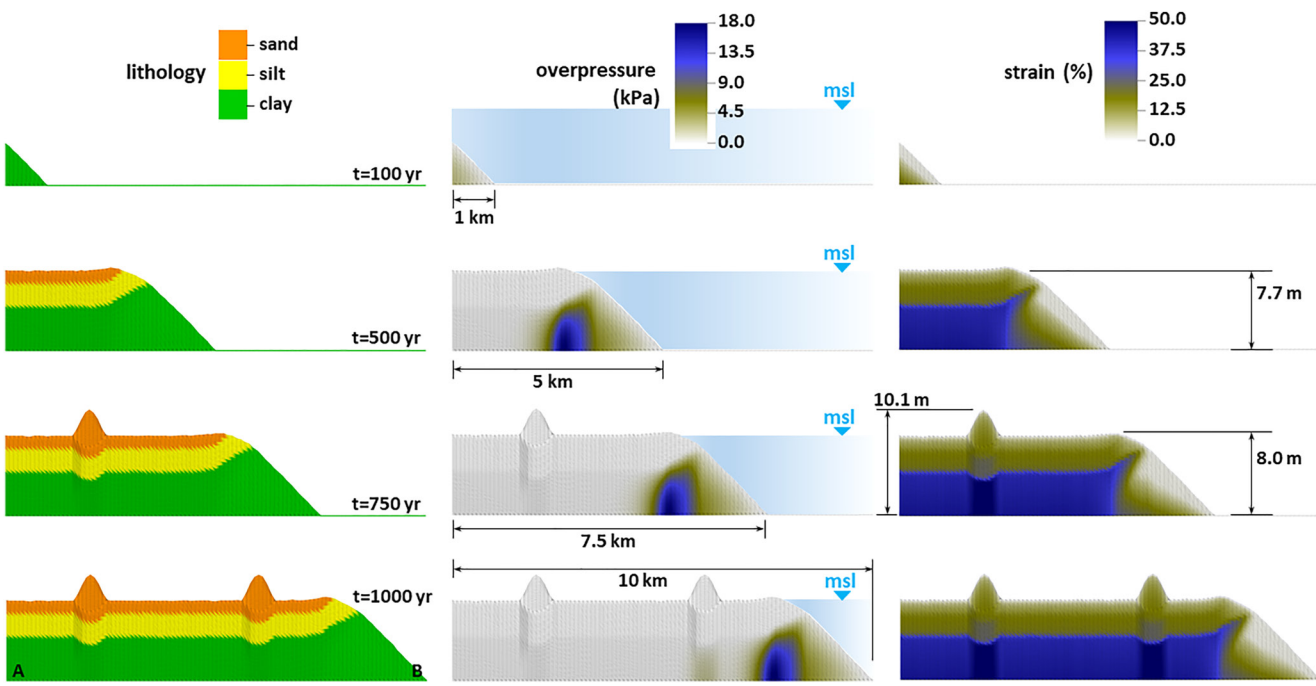

Figure 9. Delta lobe aggradation and progradation: sedimentology, overpressure, and strain along the vertical section AB traced in Figure 8 at times 100, 500, 750, and 1,000 years. Vertical exaggeration is 250.

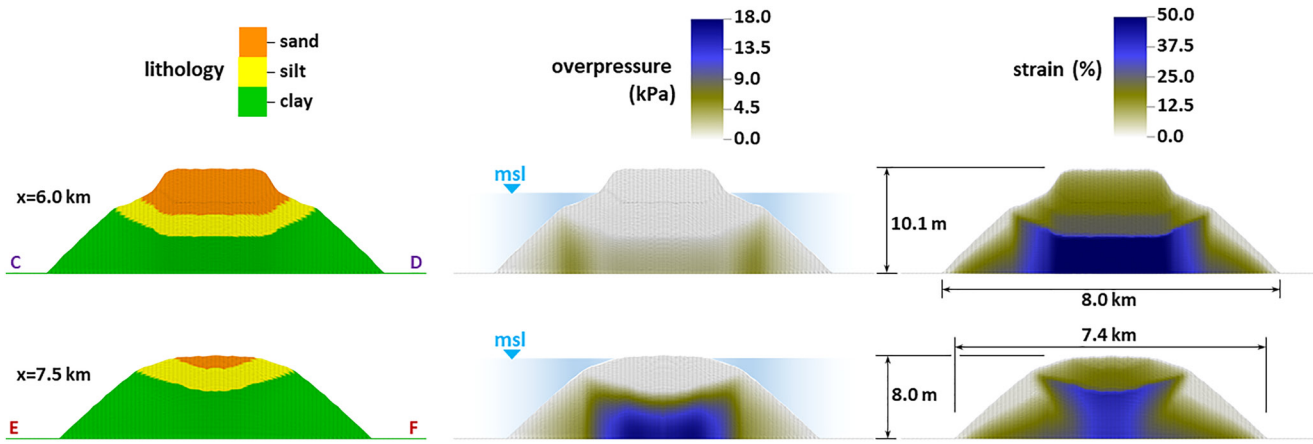

Figure 10. Delta lobe progradation: sedimentology, overpressure, and strain along the vertical sections CD and EF traced in Figure 8 at time 1,000 years. Vertical exaggeration is 250.

- the very high strain experienced by clay, ranging from 40% at the interface with the overlying silty unit to 44% at the delta floor. The value of ϵ peaks to ~52% below the dune ridges, meaning that the "original" uncompacted thickness of the clay layer is more than halved.

5. Discussion

5.1. Variability of Compaction in Depositional Environments

The important role exerted on the evolution of depositional landforms by compaction of shallow (Holocene) soils due to their own weight, also termed autocompaction (Pizzuto & Schwendt, 1997) or syn-sedimentary (Nooren et al., 2020) compaction, has been recognized by a number of authors since the mid 1900s (Kaye & Barghoorn, 1964).

The majority of these studies are aimed to investigate the past evolution of these lowlying environments and improve the quantification of long-term sea-level variations (Brain, 2016; Pizzuto & Schwendt, 1997; van Asselen et al., 2011; Vespremeanu-Stroe et al., 2017) and short-term changes in sea storminess (Bunzel et al., 2021). For example, Pizzuto and Schwendt (1997) demonstrated that at Wolfe Glade, a Delaware salt marsh, "the rate of lowering due to autocompaction alone has been one-half to one-third of the rate of SLR during most of the past 6,000 years." Understanding how much of the present land subsidence affecting lowland river floodplains and deltas is caused by natural or anthropogenic processes is another research field, often targeting compaction of Holocene deposits (Liu et al., 2021; Teatini et al., 2011; Törnqvist et al., 2008; Zoccarato et al., 2018). In the Yellow River delta, Liu et al. (2021) showed that the "long-term settlement (in a decade-to-century scale) is primarily driven by the compaction of river sediments. The more the delta sub-lobe was newly formed, the more significant the settlement."

Conversely, in a large part of the publications focused to predict the future evolution of these environments and their resilience to climate change, specifically SLR, compaction is neglected in the modeling framework or lumped into an aggregate land subsidence or relative SLR forcing term. Moreover, this contribution is always assumed constant in time, that is, over decades to centuries, and in space, on domains extended from tidal marshes (D'Alpaos & Marani, 2016; Mariotti & Canestrelli, 2017; Best et al., 2018) to entire deltas (Schmitt et al., 2021).

Our results from the application of NATSUB3D on typical scales ranging from a few tens of meters to hundreds of kilometers highlight that compaction of depositional landforms is significant and largely variable in time and space. Compaction varies in relation to the variability of the sedimentation rate and the sediment type. The heterogeneous nature of the shallow Holocene deposits has been reported by several authors (Chamberlain et al., 2018; Koster et al., 2018; Tanabe et al., 2003; Tosi et al., 2018; Vespremeanu-Stroe et al., 2017; Zecchin et al., 2008). Figures 11–13 show a combined view of sedimentology and strain along the vertical cross sections of the marsh, oxbow lake, and delta lobe cases, respectively. Elevation and strain at some representative points are included to quantitatively highlight the effect of sedimentology variability on compaction.

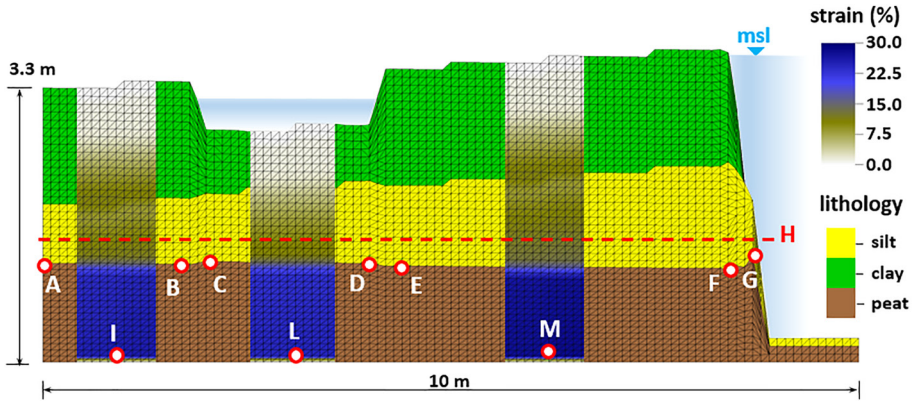

Node	Elevation (m)	Node	Strain (%)
A	1.21	I	25.9
B	1.19	L	24.8
C	1.24	M	28.5
D	1.21		
E	1.17		
F	1.12		
G	1.31		
H	1.50		

Figure 11. Thickening of the sedimentary body of a tidal marsh: model solution in terms of alternated columns showing lithology and strain along the vertical section traced in Figure 4 at time 3,000 years. Elevation and strain for a few representative points are provided on the right table. The dashed red line (with H mark) provided the "potential" thickness of the bottom peat layer without considering compaction.

For the tidal marsh (Figure 11), the bottom peat unit compacts significantly due to the load exerted by the overlying inorganic layers. A smaller compaction is computed in correspondence with the depression (24.8%, point L) compared to the remaining part of the marsh (e.g., 25.9% and 28.5%, points I and M, respectively) due to the lower load. The consequential effect is that, at the end of the simulated period, the peat layer remains a few centimeters thicker below the depression (points C and D) with respect to the other portions of the marsh (points B and E). Also notice that the larger sedimentation rates of inorganic deposits at the marsh-creek boundary (point F) causes a difference of the elevation of the peat top equal to about 0.1 m with respect to the inner boundary most distal from the creek (point A).

Comparison between the model solution at points A and B, Figure 12, points out how the lighter peat filling in part the oxbow lake is responsible for a smaller strain of the bottom of the sandy unit, that is, 11.3% versus 16.2%. Peat is more compressible than clay (Table 1), which resulted in a smaller ϵ at point D (18.5%, within a clay lens) than at the overlying point E (19.1%, within a peat lens). The higher compressibility of the oxbow lake infill with respect to the surrounding sandy deposits causes a final elevation difference between points F and G equal to 0.25 cm, that is, approximately 10% of the total thickness of the simulated domain. This causes the typical depression in surface elevation associated with buried palaeochannels in a fluvial landscape (Toonen et al., 2012).

When the total thickness of the unconsolidated deposits increases, as assumed in the delta lobe progradation case, strain may increase to even larger values than those of the previous two cases (i.e., more than 40% (point F, Figure 13)). Notice the much smaller value (24.5%) at point H due to the lack of a substantial sandy layer at the surface and overpressure still present in the clay unit (Figure 9). The delayed (relative to sedimentation) dissipation of porous overpressure can cause delayed compaction and land subsidence. This process is especially

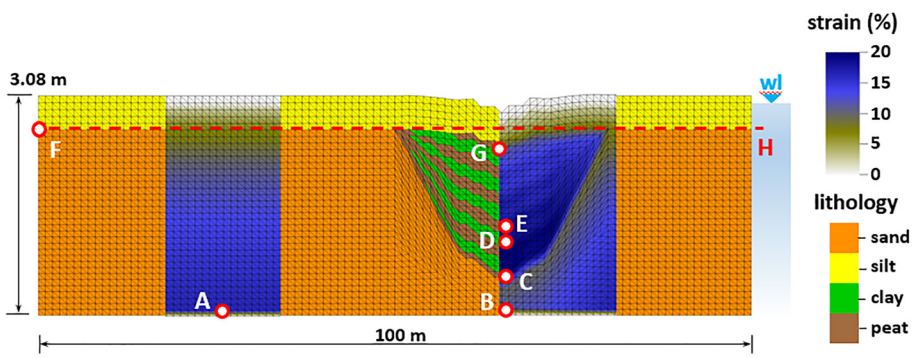

Node	Strain (%)	Node	Elevation (m)
A	16.2	F	2.60
B	11.3	G	2.35
C	20.3	H	2.63
D	18.5		
E	19.1		

Figure 12. Oxbow lake infill: model solution in terms of alternated columns showing lithology and strain along the vertical section traced in Figure 6 at time 2,200 years. Vertical exaggeration is 10. Elevation and strain for a few representative points are provided on the right table. The dashed red line (with H mark) provided the "potential" thickness of the bottom sand layer without considering compaction due to the overlying silty unit.

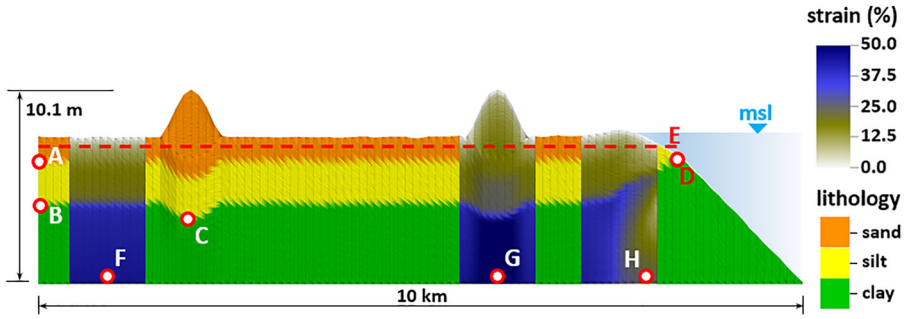

Node	Elevation (m)	Node	Strain (%)
A	6.50	F	43.7
B	4.20	G	51.9
C	3.50	H	24.5
D	6.57		
E	7.33		

Figure 13. Delta lobe progradation: model solution in terms of alternated columns showing lithology and strain along the vertical section AB traced in Figure 8 at time 1,000 years. Vertical exaggeration is 250. Elevation and strain for a few representative points are provided on the right table. The dashed red line (with E mark) provided the "potential" thickness of the bottom clay layer without considering compaction.

apparent in sediments deposited recently with high sedimentation rates, for example, at a prograding delta shore, and where underlying Holocene deposits are thick and lowly permeable, as in the Mekong delta (Zoccarato et al., 2018). Notice that, consistent with the section parallel to the main distributary of the Lafourche subdelta, Mississippi River, by Chamberlain et al. (2018), the smaller load associated with the thinner upper (sand and silt) deposits causes the deep clay unit to be shallower toward the delta front. In our case, point D is about 2.4 m higher than point B. It is also interesting to notice the effect exerted on the underlying units by the overload represented by the sand ridges. Strain at the lobe base increases to about 52% (point G), resulting in a lowering of the elevation of the interface between clay and silty layers (point C) by an additional 0.7 m. The effect of sand ridges in terms of local larger or prolonged land subsidence has been observed by Nooren et al. (2020). They noted that differential subsidence of 1–1.5 m in the Tabasco Delta, southern Mexico, is caused by syn-sedimentary delta-subsurface compaction of buried strata in response to the accumulating overburden of a prograding beach-ridge complex.

We are aware that the three case studies used to show the potential of NATSUB3D are characterized by some simplifications in the space and/or depth distribution of sediments. On one side, we observe that NATSUB3D keeps the capability of the previous 2D approach to manage extremely heterogeneous soils (Zoccarato & Teatini, 2017), with the sedimentology of the deposits that can vary in space and time at the same discretization level used to integrate Equation 1. On the other hand, this means that in real-world landforms compaction is even more heterogeneous than the results presented here.

5.2. Time Evolution of Compaction

The use of NATSUB3D allows to follow the geomorphological evolution of a landform over time, and simulate its dynamic hydrogeological parameters, that is, ϕ, c_b, and K, and spatio-temporal evolution of its state variables, that is, p, σ_z, and ϵ.

The depositional age of deposits at a specific stratigraphical position is important information to quantify, for example, post-depositional lowering (van Gorp et al., 2020) and temporal behavior of (past) SLR (Brain et al., 2015; van Asselen et al., 2011). Figure 14 provides a comprehensive view of the evolution of the three case studies with time by representing the age (in year before the simulation end (BP)) of each grid element at the last simulated time along the sections traced in Figures 5, 7 and 9.

The behavior of strain and overpressure with time in three representative points for each case study is shown in Figure 15. Figure 15a refers to three points of clayey sediments deposited on the marsh surface at the same time, about 600 years BP. Strain and overpressure increase over time to a significant difference in relative elevation, as to whether the point is below the pond where a smaller sedimentation takes place or not. Strain in locations A and C suddenly increases at $t \sim 2{,}840$ years when the effective stress overcomes $\sigma_{z,e}$. It is interesting to notice that overpressure dissipates a bit faster in point C than in A, due to C proximity to the tidal creek. However, due to the overall small p values, which is related to the small ω, the strain behavior experienced by the two points overlaps. Figure 15b shows the ϵ and p behavior versus time for three points along the vertical alignment through the deepest part of the oxbow lake. Strain and overpressure dynamics are regulated by the alternating sedimentation of (heavy) clay and (light) peat sediments. The largest changes develop during the fast sedimentation of the

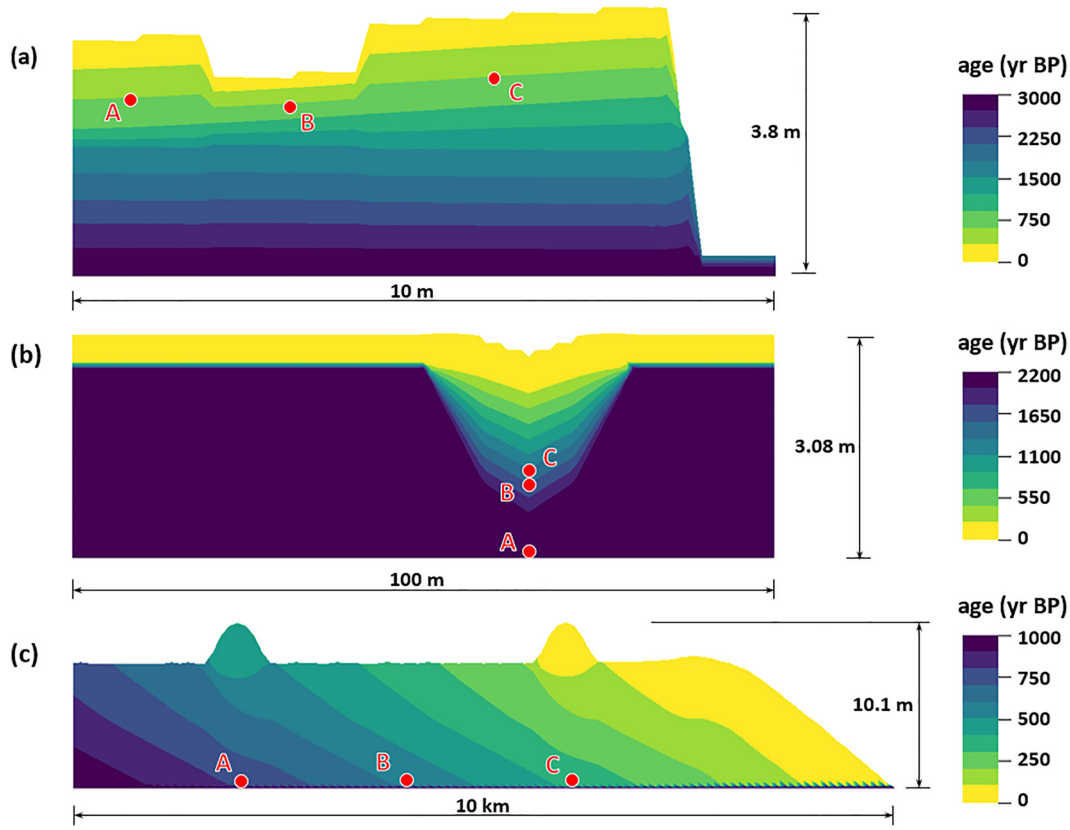

Figure 14. Evolution versus time of simulated case studies as presented by plotting the age (in year BP) of each grid element at the end of the simulation interval: (a) thickening of the sedimentary body of a tidal marsh; (b) infill on an oxbow lake; and (c) progradation of a delta lobe.

overlying silty unit. This causes an abrupt overpressure jump in the infilling material. The p dissipation between t = 2,100 years and t = 2,200 years amounts to ~5%–45% of the maximum value, suggesting that compaction will continues for decades. The strain and overpressure in the sandy deposits below the oxbow lake is negligibly affected by the lake infilling, however it is affected considerably by the deposition of the silty overburden, although with smaller values than reached in the infill. p continuously increases in the underlying sandy deposits during the last 100 years, meaning the overpressure dissipates faster in the overlying oxbow infill. The reason for this unexpected behavior lies in the fact that groundwater flow only happens in vertical direction in the sandy deposits (due to the prescribed boundary conditions) while for the infill deposits it develops "radially" into the surrounding sands. Figure 15c shows the time behavior of ϵ and p for three selected points at the base of the lobe, two of them located below beach ridges. The dynamics for the selected points are similar (identical for locations A and C), with a temporal shift following the delta progradation. As expected, strain and overpressure increases over the 250 years-long sedimentation phase. However, location B clearly highlights how p needs about 170 years after the active sedimentation phase to be fully dissipated. Strain continues to increase throughout this post-depositional phase. Notice in the profiles of locations A and C the secondary peak related to the deposition of the beach ridge.

5.3. Compaction as Driving Process of Depositional Environment Evolution

A main input to NATSUB3D is the distribution of sedimentation rate (ω) and sediment type in space and time. In this contribution aimed at pointing out the features of the novel subsurface model, ω has been specified through simplified functions. In our viewpoint NATSUB3D represents a module that could be effectively coupled to surface morphodynamic simulators, for example, DELFT3D (https://oss.deltares.nl/web/delft3d), TELEMAC-MASCARET (http://www.opentelemac.org/), or other research simulators addressing the evolution of more specific depositional environments but neglecting soil compaction (Cosma et al., 2021; Kim et al., 2009).

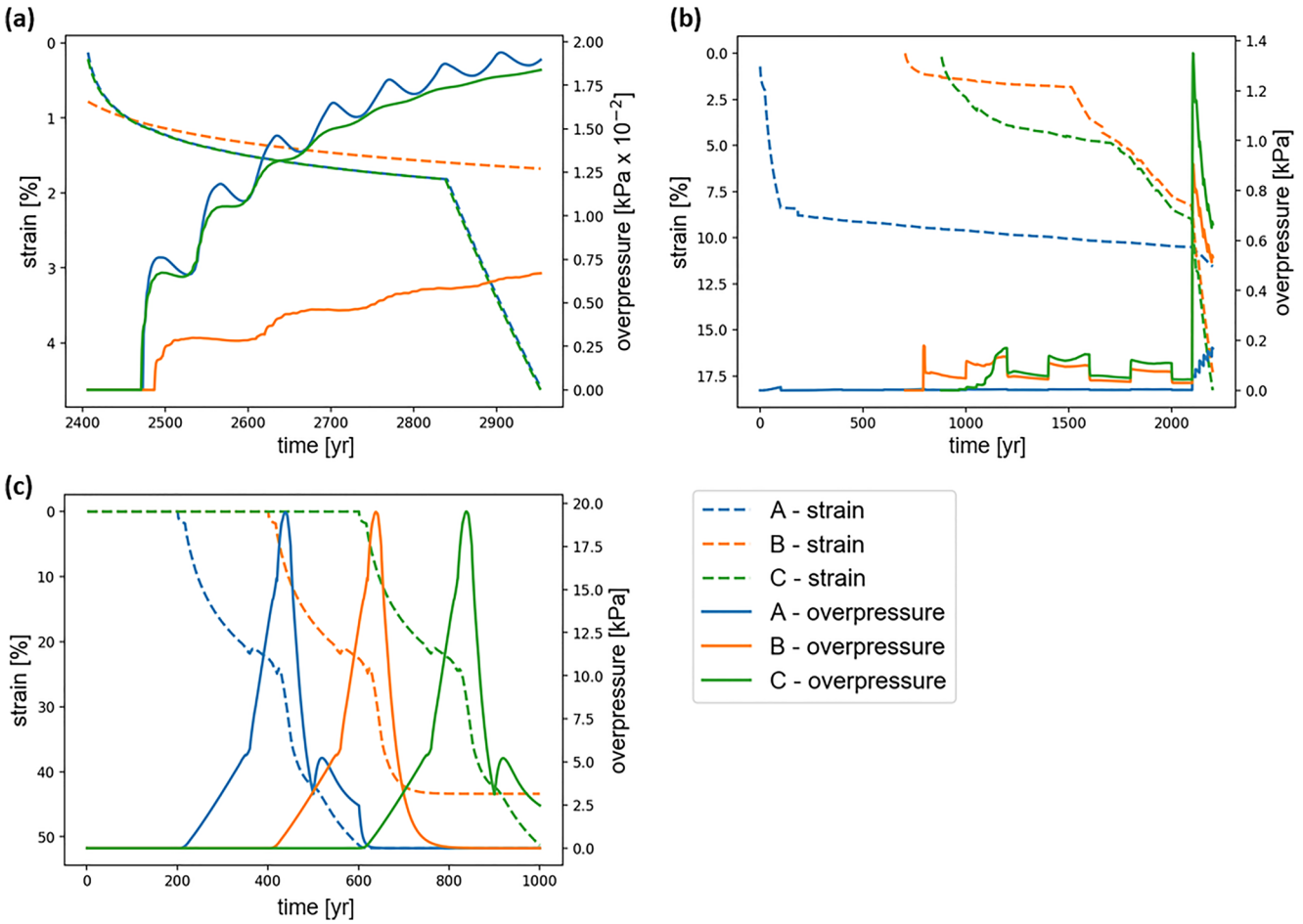

Figure 15. Strain and overpressure versus time in three representative locations for each simulated case study: (a) tidal marsh thickening; (b) oxbow lake infill; and (c) delta progradation. The point locations are provided in Figure 14.

This will improve the available tools to understand the dynamics of depositional landscapes, as well as increase our ability to quantify processes that drive their evolution. The importance of coupled surface-subsurface analyses has been recently demonstrated by coupling the 2D version of our simulator to a bio-morphological model of tidal marshes (Zoccarato et al., 2019). The need to overcome this main limitation, that is, over-simplification of subsurface processes, in high-resolution, physics-based numerical modeling of salt marsh and delta evolution has been recently pointed out by Fagherazzi et al. (2020) and Hoitink et al. (2020), respectively. The former reported that "the model has to include stratigraphic information and take into account the depositional history of organic, cohesive, and noncohesive layers …. Moreover, this approach does not account for spatial variations in sediment compaction. Spatially explicit models can solve for spatially varying subsidence, by including a mechanic module for soil compaction and recording stratigraphic information." With respect to deltas, Hoitink et al. (2020) noted that "subsidence rates from compacting coastal deposits near the sediment surface, which are spatially and temporally variable, tend to dominate the eustatic sea level rise and delta-wide, deep-seated subsidence rates during the Holocene on the worlds large deltas. Indeed, shallow river delta sediments range from well packed to extremely diffuse. Hence, the behavior of coastal sediments may exert a primary control on delta morphodynamics through the rates, which they compact."

6. Conclusion

We present a novel physics-based model to reproduce the 3D evolution of depositional landforms accounting for soil compaction. The model simulates the main hydro-geomechanical processes following sediment deposition, that is, landform evolution, dissipation of pore water over-pressure, and soil compaction. The model is

implemented according to the large strain theory by using adaptive meshes: the grid elements deform following the grain movement and increase in number to account for landform growth due to sedimentation. Terzaghi's theory governs soil compaction, with the hydro-geomechanical properties, that is, compressibility, hydraulic conductivity, porosity, depending on the sediment type and the vertical effective stress.

Applying this model to realistic case studies, we derive the following conclusions:

- The compaction of shallow soils significantly influences the vertical development of depositional landforms. The high porosity and compressibility typical of recently deposited sedimentary soils favor the occurrence of large strain that can amount up to 50% when soft sediments (i.e., clay and peat) become buried by younger sediments. A dynamic mesh is required to follow the physical process.
- With respect to a previous 2D formulation, the 3D framework proposed allows a proper representation of the evolution of complex geometric and sedimentary settings. Moreover, the model is able to automatically adjust the integration temporal step to the actual sedimentation rates and to reconstruct heterogeneous sediment distributions. This latter results are particularly important for understanding uneven elevation of landform surfaces.
- Compaction must be considered when developing reliable interpretations and predictions of past and future, respectively, resilience of lowlying coastal landforms. Simple geometric quantification of landform volume neglecting stress-dependent compaction can result in a serious underestimation of (a) the sediment mass required to build-up the landform in the actual shape, and (b) the present sedimentation rate needed for a landform's elevation to keep pace with rising sea level.

In sum, this work presents a new tool that increases our capability to develop more reliable insights on the evolution of depositional environments. In this contribution we focused the attention on the evolution of natural landforms and gradual sedimentation events, however the simulator can also be used in coastal restoration projects where large amounts of sediment are deposited in a short time period and overpressure consequently spikes to high values. Moreover, NATSUB3D is intrinsically suitable to be coupled with surficial morphodynamic simulators that quantify spatial, temporal, and variability of deposition rate and sediment type on the landform surface. Finally, NATSUB3D will be updated to account for other processes governing the compaction and the evolution of hydro-geomechanical properties of shallow deposits, such as secondary consolidation (or creep), organic matter bio-degradation, desiccation, and anthropogenic drainage.

Data Availability Statement

The NATSUB3D simulator and modeling inputs for the three cases described in this manuscript are published online at https://doi.org/10.4211/hs.83c2ac39fced4ab98ca7c2b5e6706261 (Xotta et al., 2022), available via Creative Commons Attribution BY-NC 4.0 International Public License.

Acknowledgments
This article is an outcome of the Research Project HIETE ("The Holocene Imprint on the future Evolution of Transitional Environments") funded by Fondazione CARIPARO and of the VENEZIA-2021 Research Programme, Topic 3.1, funded by the "Provveditorato Interregionale Opere Pubbliche per il Veneto, Trentino Alto Adige e Friuli Venezia Giulia" through the "Concessionario Consorzio Venezia Nuova" and coordinated by CORILA, Venice. Philip Minderhoud received funding from the European Union's Horizon 2020 research and innovation programme under the Marie Skłodowska-Curie grant agreement No 894476—InSPiRED—H2020-MSCA-IF-2019. All data used in this study are described in the article and the supplementary material.

References

Allen, J. R. L. (1999). Geological impact on coastal wetland landscapes: Some general effects of sediment autocompaction in the Holocene of northwest Europe. *The Holocene*, *9*(1), 1–12. https://doi.org/10.1191/095968399674929667 2

Allen, J. R. L. (2000). Morphodynamics of Holocene salt marshes: A review sketch from the Atlantic and Southern North Sea coasts of Europe. *Quaternary Science Reviews*, *19*(12), 1155–1231. https://doi.org/10.1016/s0277-3791(99)00034-7

Amorosi, A., Bruno, L., Campo, B., Costagli, B., Dinelli, E., Hong, W., et al. (2020). Tracing clinothem geometry and sediment pathways in the prograding Holocene Po Delta system through integrated core stratigraphy. *Basin Research*, *32*(2), 206–215. https://doi.org/10.1111/bre.12360

Audet, D., & Fowler, A. (1992). A mathematical model for compaction in sedimentary basins. *Geophysical Journal International*, *110*(3), 577–590. https://doi.org/10.1111/j.1365-246X.1992.tb02093.x

Bahr, D. B., Hutton, E. W., Syvitski, J. P., & Pratson, L. F. (2001). Exponential approximations to compacted sediment porosity profiles. *Computers & Geosciences*, *27*(6), 691–700. https://doi.org/10.1016/S0098-3004(00)00140-0

Barbier, E. B., Hacker, S. D., Kennedy, C., Koch, E. W., Stier, A. C., & Silliman, B. R. (2011). The value of estuarine and coastal ecosystem services. *Ecological Monographs*, *81*(2), 169–193. https://doi.org/10.1890/10-1510.1

Best, U. S. N., Van der Wegen, M., Dijkstra, J., Willemsen, P. W. J. M., Borsje, B. W., & Roelvink, D. J. A. (2018). Do salt marshes survive sea level rise? Modelling wave action, morphodynamics and vegetation dynamics. *Environmental Modelling & Software*, *109*, 152–166. https://doi.org/10.1016/j.envsoft.2018.08.004

Bogoni, M., Putti, M., & Lanzoni, S. (2017). Modeling meander morphodynamics over self-formed heterogeneous floodplains. *Water Resources Research*, *53*(6), 5137–5157. https://doi.org/10.1002/2017WR020726

Brain, M. J. (2016). Past, present and future perspectives of sediment compaction as a driver of relative sea level and coastal change. *Current Climate Change Reports*, *2*(3), 75–85. https://doi.org/10.1007/s40641-016-0038-6

Brain, M. J., Kemp, A. C., Horton, B. P., Culver, S. J., Parnell, A. C., & Cahill, N. (2015). Quantifying the contribution of sediment compaction to late Holocene salt-marsh sea-level reconstructions, North Carolina, USA. *Quaternary Research*, *83*(1), 41–51. https://doi.org/10.1016/j.yqres.2014.08.003

Brain, M. J., Long, A. J., Petley, D. N., Horton, B. P., & Allison, R. J. (2011). Compression behaviour of minerogenic low energy intertidal sediments. *Sedimentary Geology*, *233*(1–4), 28–41. https://doi.org/10.1016/j.sedgeo.2010.10.005

Brain, M. J., Long, A. J., Woodroffe, S. A., Petley, D. N., Milledge, D. G., & Parnell, A. C. (2012). Modelling the effects of sediment compaction on salt marsh reconstructions of recent sea-level rise. *Earth and Planetary Science Letters*, *345–348*, 180–193. https://doi.org/10.1016/j.epsl.2012.06.045

Bredehoeft, J. D., & Hanshaw, B. B. (1968). On the maintenance of anomalous fluid pressures: I. Thick sedimentary sequences. *GSA Bulletin*, *79*(9), 1097–1106. https://doi.org/10.1130/0016-7606(1968)79[1097:otmoaf]2.0.co;2

Bridge, J. S. (2003). *Rivers and floodplains: Forms, processes, and sedimentary record*. John Wiley & Sons.

Bridgeman, J. G. (2018). *Understanding Mississippi delta subsidence through stratigraphic and geotechnical analysis of a continuous Holocene core at a subsidence superstation*. Tulane University. Retrieved from https://digitallibrary.tulane.edu/islandora/object/tulane%3A78959

Bunzel, D., Milker, Y., Müller-Navarra, K., Arz, H. W., & Schmiedl, G. (2021). North Sea salt-marsh archives trace past storminess and climate variability. *Global and Planetary Change*, *198*, 103403. https://doi.org/10.1016/j.gloplacha.2020.103403

Chamberlain, E. L., Törnqvist, T. E., Shen, Z., Mauz, B., & Wallinga, J. (2018). Anatomy of Mississippi Delta growth and its implications for coastal restoration. *Science Advances*, *4*(4), eaar4740. https://doi.org/10.1126/sciadv.aar4740

Constantine, J. A., Dunne, T., Piégay, H., & Kondolf, M. (2010). Controls on the alluviation of oxbow lakes by bed-material load along the Sacramento River, California. *Sedimentology*, *57*(2), 389–407. https://doi.org/10.1111/j.1365-3091.2009.01084.x

Cosma, M., Yan, N., Colombera, L., Mountney, N. P., D'Alpaos, A., & Ghinassi, M. (2021). An integrated approach to determine three-dimensional accretion geometries of tidal point bars: Examples from the Venice Lagoon (Italy). *Sedimentology*, *68*(1), 449–476. https://doi.org/10.1111/sed.12787

D'Alpaos, A., & Marani, M. (2016). Reading the signatures of biologic–geomorphic feedbacks in salt-marsh landscapes. *Advances in Water Resources*, *93*, 265–275. https://doi.org/10.1016/j.advwatres.2015.09.004

Davis, R. (2013). 10.16 Evolution of coastal landforms. In J. F. Shroder (Ed.), *Treatise on geomorphology* (pp. 417–448). Academic Press. https://doi.org/10.1016/B978-0-12-374739-6.00293-1

Dunne, T., & Aalto, R. (2013). 9.32 Large river floodplains. In J. F. Shroder (Ed.), *Treatise on geomorphology* (pp. 645–678). Academic Press. https://doi.org/10.1016/B978-0-12-374739-6.00258-X

Ericson, J. P., Vörösmarty, C. J., Dingman, S. L., Ward, L. G., & Meybeck, M. (2006). Effective sea-level rise and deltas: Causes of change and human dimension implications. *Global and Planetary Change*, *50*(1), 63–82. https://doi.org/10.1016/j.gloplacha.2005.07.004

Fagherazzi, S., Kearney, W., Mariotti, G., Leonardi, N., & Nardin, W. (2021). Understanding marsh dynamics: Modeling approaches. In D. M. Fitzgerald, & Z. J. Hughes (Eds.), *Salt marshes: Function, dynamics, and stresses* (pp. 278–299). Cambridge University Press. https://doi.org/10.1017/9781316888933.013

Fagherazzi, S., Mariotti, G., Leonardi, N., Canestrelli, A., Nardin, W., & Kearney, W. S. (2020). Salt marsh dynamics in a period of accelerated sea level rise. *Journal of Geophysical Research: Earth Surface*, *125*(8), e2019JF005200. https://doi.org/10.1029/2019JF005200

Gambolati, G. (1973a). Equation for one-dimensional vertical flow of groundwater. 1. The rigorous theory. *Water Resources Research*, *9*(4), 1022–1028. https://doi.org/10.1029/wr009i004p01022

Gambolati, G. (1973b). Equation for one-dimensional vertical flow of groundwater. 2. Validity range of the diffusion equation. *Water Resources Research*, *9*(5), 1385–1395. https://doi.org/10.1029/wr009i005p01385

Gambolati, G., Giunta, G., & Teatini, P. (1998). Numerical modeling of natural land subsidence over sedimentary basins undergoing large compaction. In G. Gambolati (Ed.), *CENAS–coastline evolution of the upper Adriatic Sea due to sea level rise and natural and anthropogenic land subsidence* (pp. 77–102). Klwer Academic Publications.

Gibson, R. E. (1958). The progress of consolidation in a clay layer increasing in thickness with time. *Geotechnique*, *8*(4), 171–182. https://doi.org/10.1680/geot.1958.8.4.171

Gibson, R. E., Schiffman, R. L., & Cargill, K. W. (1981). The theory of one-dimensional soil consolidation of saturated clays, II. Finite non-linear consolidation of thin homogeneous layers. *Canadian Geotechnical Journal*, *18*(2), 280–293. https://doi.org/10.1139/t81-030

Hoitink, A. J. F., Nittrouer, J. A., Passalacqua, P., Shaw, J. B., Langendoen, E. J., Huismans, Y., & van Maren, D. S. (2020). Resilience of river deltas in the Anthropocene. *Journal of Geophysical Research: Earth Surface*, *125*(3), e2019JF005201. https://doi.org/10.1029/2019JF005201

Hudson, P. F., & Kesel, R. H. (2000). Channel migration and meander-bend curvature in the lower Mississippi River prior to major human modification. *Geology*, *28*(6), 531–534. https://doi.org/10.1130/0091-7613(2000)028<0531:cmambc>2.3.co;2

Ishii, Y., & Hori, K. (2016). Formation and infilling of oxbow lakes in the Ishikari lowland, northern Japan. *Quaternary International*, *397*, 136–146. https://doi.org/10.1016/j.quaint.2015.06.016

Jankowski, K. L., Törnqvist, T. E., & Fernandes, A. M. (2017). Vulnerability of Louisiana's coastal wetlands to present-day rates of relative sea-level rise. *Nature Communications*, *8*(1), 14792. https://doi.org/10.1038/ncomms14792

Kaye, C. A., & Barghoorn, E. S. (1964). Late Quaternary sea-level change and crustal rise at Boston, Massachusetts, with notes on the autocompaction of peat. *GSA Bulletin*, *75*(2), 63–80. https://doi.org/10.1130/0016-7606(1964)75[63:lqscac]2.0.co;2

Keogh, M. E., & Törnqvist, T. E. (2019). Measuring rates of present-day relative sea-level rise in low-elevation coastal zones: A critical evaluation. *Ocean Science*, *15*(1), 61–73. https://doi.org/10.5194/os-15-61-2019

Kim, W., Dai, A., Muto, T., & Parker, G. (2009). Delta progradation driven by an advancing sediment source: Coupled theory and experiment describing the evolution of elongated deltas. *Water Resources Research*, *45*(6), W06428. https://doi.org/10.1029/2008WR007382

Koster, K., Stafleu, J., & Stouthamer, E. (2018). Differential subsidence in the urbanised coastal-deltaic plain of The Netherlands. *Netherlands Journal of Geosciences*, *97*(4), 215–227. https://doi.org/10.1017/njg.2018.11

Lambe, T. W., & Whitman, R. V. (1969). *Soil mechanics*. John Wiley & Sons.

Liu, Y., Liu, J., Xia, X., Bi, H., Huang, H., Ding, R., & Zhao, L. (2021). Land subsidence of the Yellow River Delta in China driven by river sediment compaction. *Science of the Total Environment*, *750*, 142165. https://doi.org/10.1016/j.scitotenv.2020.142165

Marani, M., D'Alpaos, A., Lanzoni, S., Carniello, L., & Rinaldo, A. (2010). The importance of being coupled: Stable states and catastrophic shifts in tidal biomorphodynamics. *Journal of Geophysical Research*, *115*(F4), F04004. https://doi.org/10.1029/2009JF001600

Mariotti, G., & Canestrelli, A. (2017). Long-term morphodynamics of muddy backbarrier basins: Fill in or empty out? *Water Resources Research*, *53*(8), 7029–7054. https://doi.org/10.1002/2017WR020461

Massey, A. C., Paul, M. A., Gehrels, W. R., & Charman, D. J. (2006). Autocompaction in Holocene coastal back-barrier sediments from south Devon, southwest England, UK. *Marine Geology*, *226*(3–4), 225–241. https://doi.org/10.1016/j.margeo.2005.11.003

Meckel, T. A., Ten Brink, U. S., & Williams, S. J. (2007). Sediment compaction rates and subsidence in deltaic plains: Numerical constraints and stratigraphic influences. *Basin Research*, *19*(1), 19–31. https://doi.org/10.1111/j.1365-2117.2006.00310.x

Mesri, G., & Vardhanabhuti, B. (2009). Compression of granular materials. *Canadian Geotechnical Journal*, *64*(4), 369–392. https://doi.org/10.1139/T08-123

Milliman, J. D., & Farnsworth, K. (2011). *River discharge to the coastal ocean: A global synthesis*. Cambride University Press.

Minderhoud, P. S. J., Cohen, K. M., Toonen, W. H. J., Erkens, G., & Hoek, W. Z. (2016). Improving age-depth models of fluvio-lacustrine deposits using sedimentary proxies for accumulation rates. *Quaternary Geochronology*, *33*, 35–45. https://doi.org/10.1016/j.quageo.2016.01.001

Moodie, A. J., Nittrouer, J. A., Ma, H., Carlson, B. N., Chadwick, A. J., Lamb, M. P., & Parker, G. (2019). Modeling deltaic lobe-building cycles and channel avulsions for the Yellow River delta, China. *Journal of Geophysical Research: Earth Surface*, *124*(11), 2438–2462. https://doi.org/10.1029/2019JF005220

Mudd, S. M., Howell, S. M., & Morris, J. T. (2009). Impact of dynamic feedbacks between sedimentation, sea-level rise, and biomass production on near-surface marsh stratigraphy and carbon accumulation. *Estuarine, Coastal and Shelf Science*, *82*(3), 377–389. https://doi.org/10.1016/j.ecss.2009.01.028

Nageswara Rao, K., Saito, Y., Nagakumar, K., Demudu, G., Rajawat, A., Kubo, S., & Li, Z. (2015). Palaeogeography and evolution of the Godavari delta, east coast of India during the Holocene: An example of wave-dominated and fan-delta settings. *Palaeogeography, Palaeoclimatology, Palaeoecology*, *440*, 213–233. https://doi.org/10.1016/j.palaeo.2015.09.006

Nooren, K., Cohen, K. M., Nienhuis, J. H., & Hoek, W. Z. (2020). Late Holocene differential subsidence and relative sea level rise in the Tabasco Delta, Mexico. *Proceedings of the International Association of Hydrological Sciences*, *382*, 149–153. https://doi.org/10.5194/piahs-382-149-2020

Pietroń, J., Nittrouer, J. A., Chalov, S. R., Dong, T. Y., Kasimov, N., Shinkareva, G., & Jarsjö, J. (2018). Sedimentation patterns in the Selenga River delta under changing hydroclimatic conditions. *Hydrological Processes*, *32*(2), 278–292. https://doi.org/10.1002/hyp.11414

Pizzuto, J. E., & Schwendt, A. E. (1997). Mathematical modeling of autocompaction of a Holocene transgressive valley-fill deposit, Wolfe Glade, Delaware. *Geology*, *25*(1), 57–60. https://doi.org/10.1130/0091-7613(1997)025<0057:mmoaoa>2.3.co;2

Schindler, S., O'Neill, F. H., Biró, M., Damm, C., Gasso, V., Kanka, R., et al. (2016). Multifunctional floodplain management and biodiversity effects: A knowledge synthesis for six European countries. *Biodiversity and Conservation*, *25*(7), 1349–1382. https://doi.org/10.1007/s10531-016-1129-3

Schmitt, R. J. P., Giuliani, M., Bizzi, S., Kondolf, G. M., Daily, G. C., & Castelletti, A. (2021). Strategic basin and delta planning increases the resilience of the Mekong Delta under future uncertainty. *Proceedings of the National Academy of Sciences of the United States of America*, *118*(36). e2026127118. https://doi.org/10.1073/pnas.2026127118

Seto, K. C. (2011). Exploring the dynamics of migration to mega-delta cities in Asia and Africa: Contemporary drivers and future scenarios. *Global Environmental Change*, *21*, S94–S107. https://doi.org/10.1016/j.gloenvcha.2011.08.005

Sheldon, N. D., & Retallack, G. J. (2001). Equation for compaction of paleosols due to burial. *Geology*, *29*(3), 247–250. https://doi.org/10.1130/0091-7613(2001)029<0247:efcopd>2.0.co;2

Syvitski, J. P., & Hutton, E. W. (2001). 2D sedflux 1.0C: An advanced process-response numerical model for the fill of marine sedimentary basins. *Computers & Geosciences*, *27*(6), 731–753. https://doi.org/10.1016/S0098-3004(00)00139-4

Syvitski, J. P. M., Vörösmarty, C. J., Kettner, A. J., & Green, P. (2005). Impact of humans on the flux of terrestrial sediment to the global coastal ocean. *Science*, *308*(5720), 376–380. https://doi.org/10.1126/science.1109454

Tanabe, S., Saito, Y., Sato, Y., Suzuki, Y., Sinsakul, S., Tiyapairach, S., & Chaimanee, N. (2003). Stratigraphy and Holocene evolution of the mud-dominated Chao Phraya delta, Thailand. *Quaternary Science Reviews*, *22*(8), 789–807. https://doi.org/10.1016/S0277-3791(02)00242-1

Teatini, P., Tosi, L., & Strozzi, T. (2011). Quantitative evidence that compaction of Holocene sediments drives the present land subsidence of the Po Delta, Italy. *Journal of Geophysical Research*, *116*(B8), B08407. https://doi.org/10.1029/2010JB008122

Terzaghi, K. (1923). Die berechnung des durchlassigkeitsziffer des tones aus dem verlauf der hydrodynamischen spannungserscheinungen. *Akademie der Wissenschaften in Wien, Sitzungsberichte, Math. Naturwiss. Klasse, Part Ha*, *132*(3–4), 125–138.

Terzaghi, K., Peck, R. B., & Mesri, G. (1996). *Soil mechanics in engineering practice*. John Wiley & Sons.

Toonen, W. H. J., Kleinhans, M. G., & Cohen, K. M. (2012). Sedimentary architecture of abandoned channel fills. *Earth Surface Processes and Landforms*, *37*(4), 459–472. https://doi.org/10.1002/esp.3189

Törnqvist, T. E., Wallace, D. J., Storms, J. E. A., Wallinga, J., van Dam, R. L., Blaauw, M., et al. (2008). Mississippi Delta subsidence primarily caused by compaction of Holocene strata. *Nature Geoscience*, *1*(3), 173–176. https://doi.org/10.1038/ngeo129

Tosi, L., Lio, C. D., Teatini, P., & Strozzi, T. (2018). Land subsidence in coastal environments: Knowledge advance in the Venice coastland by TerraSAR–X PSI. *Remote Sensing*, *10*(8), 1191. https://doi.org/10.3390/rs10081191

Tovey, K. N., & Paul, M. A. (2002). Modelling self-weight consolidation in Holocene sediments. *Bulletin of Engineering Geology and the Environment*, *61*(1), 21–33. https://doi.org/10.1007/s100640100126

van Asselen, S., Karssenberg, D., & Stouthamer, E. (2011). Contribution of peat compaction to relative sea-level rise within Holocene deltas. *Geophysical Research Letters*, *38*(24). https://doi.org/10.1029/2011GL049835

van Asselen, S., Stouthamer, E., & van Asch, T. (2009). Effects of peat compaction on delta evolution: A review on processes, responses, measuring and modeling. *Earth-Science Reviews*, *92*(1), 35–51. https://doi.org/10.1016/j.earscirev.2008.11.001

van Gorp, W., Sevink, J., & van Leusen, P. (2020). Post-depositional subsidence of the Avellino tephra marker bed in the Pontine plain (Lazio, Italy): Implications for Early Bronze Age palaeogeographical, water level and relative sea level reconstruction. *Catena*, *194*, 104770. https://doi.org/10.1016/j.catena.2020.104770

Vespremeanu-Stroe, A., Zăinescu, F., Preoteasa, L., Tătui, F., Rotaru, S., Morhange, C., et al. (2017). Holocene evolution of the Danube delta: An integral reconstruction and a revised chronology. *Marine Geology*, *388*, 38–61. https://doi.org/10.1016/j.margeo.2017.04.002

Weis, P. (2016). Salt marsh accretion. In M. J. Kennish (Ed.), *Encyclopedia of estuaries* (pp. 513–515). Springer Netherlands. https://doi.org/10.1007/978-94-017-8801-4_28

Wiberg, P. L., Fagherazzi, S., & Kirwan, M. L. (2020). Improving predictions of salt marsh evolution through better integration of data and models. *Annual Review of Marine Science*, *12*(1), 389–413. https://doi.org/10.1146/annurev-marine-010419-010610

Xotta, R., Zoccarato, C., Minderhoud, P. S. J., & Teatini, P. (2022). Software (and data) for "Modelling the role of compaction in the three-dimensional evolution of depositional environments" [Software]. Hydroshare. https://doi.org/10.4211/hs.83c2ac39fced4ab98ca7c2b5e6706261

Zecchin, M., Baradello, L., Brancolini, G., Donda, F., Rizzetto, F., & Tosi, L. (2008). Sequence stratigraphy based on high-resolution seismic profiles in the late Pleistocene and Holocene deposits of the Venice area. *Marine Geology*, *253*(3), 185–198. https://doi.org/10.1016/j.margeo.2008.05.010

Zoccarato, C., & Da Lio, C. (2021). The Holocene influence on the future evolution of the Venice Lagoon tidal marshes. *Communications Earth & Environment*, *2*(1), 1–9. https://doi.org/10.1038/s43247-021-00144-4

Zoccarato, C., Da Lio, C., Tosi, L., & Teatini, P. (2019). A coupled biomorpho-geomechanical model of tidal marsh evolution. *Water Resources Research*, *55*(11), 8330–8349. https://doi.org/10.1029/2019WR024875

Zoccarato, C., Minderhound, P. S. J., & Teatini, P. (2018). The role of sedimentation and natural compaction in a prograding delta: Insights from the mega Mekong delta, Vietnam. *Scientific Report*, *8*(1), 11437. https://doi.org/10.1038/s41598-018-29734-7

Zoccarato, C., & Teatini, P. (2017). Numerical simulations of Holocene salt-marsh dynamics under the hypothesis of large soil deformations. *Advances in Water Resources*, *110*, 107–119. https://doi.org/10.1016/j.advwatres.2017.10.006

Zoccarato, C., Törnqvist, T. E., Teatini, P., & Bridgeman, J. G. (2020). A shallow compaction model for Holocene Mississippi Delta sediments. *Proceedings of the International Association of Hydrological Sciences*, *382*, 565–570. https://doi.org/10.5194/piahs-382-565-2020